Article

Cell Reports

Structure, function, and evolution of the *Orthobunyavirus* membrane fusion glycoprotein

Graphical abstract

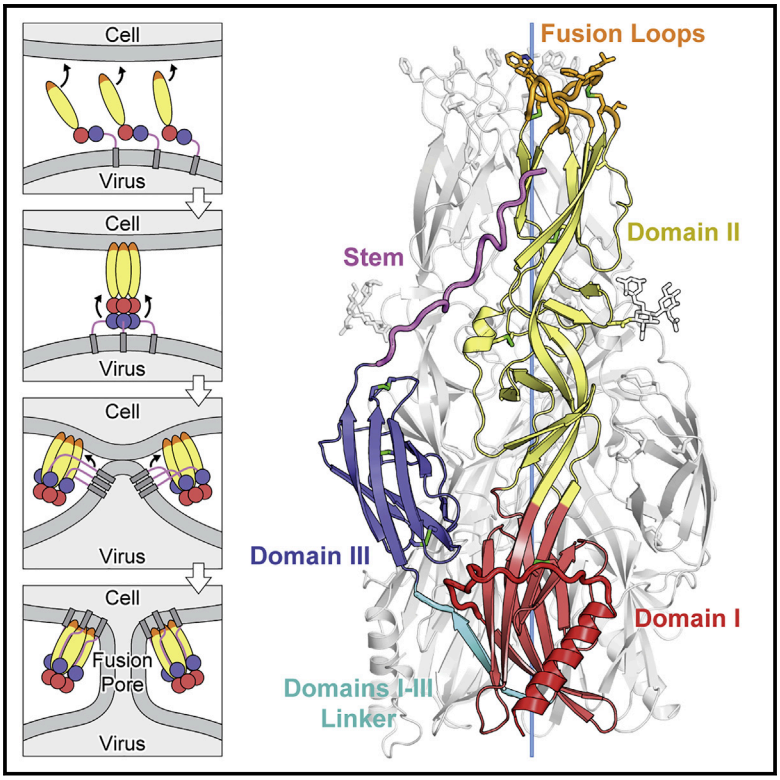

Highlights

- Structures of La Crosse and Schmallenberg virus Gc^F in its post-fusion form
- A vestigial ER translocation signal sequence links Gc^S and Gc^F in orthobunyavirus (OBV) Gc
- The host membrane insertion surface of OBV Gc is composed of three fusion loops
- Antigenic sites of Oropouche virus mapped to the OBV Gc^F trimer interface

Authors

Jan Hellert, Andrea Aebischer, Ahmed Haouz, Pablo Guardado-Calvo, Sven Reiche, Martin Beer, Félix A. Rey

Correspondence

martin.beer@fli.de (M.B.), felix.rey@pasteur.fr (F.A.R.)

In brief

Hellert et al. describe the 3D structures of the membrane fusion protein from two orthobunyaviruses, La Crosse and Schmallenberg viruses, in the conformation they adopt after completing the membrane fusion reaction. Structure-based mutagenesis identifies key residues required for their fusogenic activity, and comparison with homologs across the Bunyavirales shows evolutionary relationships.

Hellert et al., 2023, Cell Reports *42*, 112142
March 28, 2023
https://doi.org/10.1016/j.celrep.2023.112142

CellPress

Cell Reports

CellPress
OPEN ACCESS

Article

Structure, function, and evolution of the *Orthobunyavirus* membrane fusion glycoprotein

Jan Hellert,[1,2] Andrea Aebischer,[3,4] Ahmed Haouz,[5] Pablo Guardado-Calvo,[1] Sven Reiche,[4] Martin Beer,[3,*] and Félix A. Rey[1,6,*]

[1]Structural Virology Unit, Institut Pasteur – Université Paris-Cité, CNRS UMR 3569, 25-28 rue du Dr. Roux, 75015 Paris, France
[2]Centre for Structural Systems Biology (CSSB), Leibniz-Institut für Virologie (LIV), Notkestraße 85, 22607 Hamburg, Germany
[3]Institute of Diagnostic Virology, Friedrich-Loeffler-Institut, Südufer 10, 17493 Greifswald, Germany
[4]Department of Experimental Animal Facilities and Biorisk Management, Friedrich-Loeffler-Institut, Südufer 10, 17493 Greifswald, Germany
[5]Crystallography Platform C2RT, Institut Pasteur, CNRS UMR 3528, 25-28 rue du Dr. Roux, 75015 Paris, France
[6]Lead contact
*Correspondence: martin.beer@fli.de (M.B.), felix.rey@pasteur.fr (F.A.R.)
https://doi.org/10.1016/j.celrep.2023.112142

SUMMARY

La Crosse virus, responsible for pediatric encephalitis in the United States, and Schmallenberg virus, a highly teratogenic veterinary virus in Europe, belong to the large *Orthobunyavirus* genus of zoonotic arthropod-borne pathogens distributed worldwide. Viruses in this under-studied genus cause CNS infections or fever with debilitating arthralgia/myalgia syndromes, with no effective treatment. The main surface antigen, glycoprotein Gc (~1,000 residues), has a variable N-terminal half (Gc^S) targeted by the patients' antibody response and a conserved C-terminal moiety (Gc^F) responsible for membrane fusion during cell entry. Here, we report the X-ray structure of post-fusion La Crosse and Schmallenberg virus Gc^F, revealing the molecular determinants for hairpin formation and trimerization required to drive membrane fusion. We further experimentally confirm the role of residues in the fusion loops and in a vestigial endoplasmic reticulum (ER) translocation sequence at the Gc^S-Gc^F junction. The resulting knowledge provides essential molecular underpinnings for future development of potential therapeutic treatments and vaccines.

INTRODUCTION

Emerging viral zoonoses pose serious threats to human health worldwide.[1] With more than 100 recorded viral species,[2,3] the *Orthobunyavirus* (OBV) genus of the *Peribunyaviridae* family in the *Bunyavirales* order is the largest group of arboviruses sharing the same particle organization and replication machinery. Most medically important viruses in the OBV genus belong to the Bunyamwera, California, or Simbu serocomplexes. They are responsible for a wide spectrum of diseases. Mosquito-transmitted OBVs in the California serogroup cause neurological disease in humans in North America,[4] and infection with the most studied member of this serogroup, La Crosse virus (LACV), leads to long-term cognitive deficits in approximately 10% of symptomatic children.[5] In South America, Oropouche virus (OROV) of the Simbu serocomplex, transmitted by mosquitoes or midges, causes systemic infection with symptoms related to Chikungunya or Dengue disease, caused by better-studied viruses from the *Alphavirus* and *Flavivirus* genera, respectively. This situation leads to frequent misdiagnosis of Oropouche disease.[6,7] In sub-Saharan Africa, mosquito-borne Ngari virus (NRIV) of the Bunyamwera serocomplex has caused large outbreaks of viral hemorrhagic fever, initially misdiagnosed as Rift Valley fever disease.[8,9] Other non-zoonotic OBVs, such as Akabane virus (AKAV) or Schmallenberg virus (SBV) from the Simbu serocomplex, are well known for their severe teratogenic effects in ruminants.[10]

The OBV genome is composed of three segments—large (L), medium (M), and small (S)—of single-stranded RNA of negative polarity.[2] The genomic segments are coated with the nucleoprotein N,[11,12] encoded in segment S. The ends of each segment are bound to the viral polymerase,[13] encoded in segment L, to form genomic ribonucleoprotein (RNP) complexes. The surface glycoproteins Gn and Gc are proteolytically derived from a polyprotein precursor encoded in segment M.[14,15] When two related OBVs infect the same cell, the progeny virus can contain segments from both parent viruses; i.e., a reassorted genome. The reassorted progeny can have different tropism and/or antigenicity, as seen frequently in other viruses with segmented genomes;[16] for example, influenza A virus[17] as well as viruses in other families in the *Bunyavirales* order.[18] The abovementioned NRIV, which emerged in Africa in the 1990s causing hemorrhagic fever in humans, was later shown to be a reassortant having the L and S segments of Bunyamwera virus (BUNV, the OBV type species) and the M segment of Batai virus (BATV; also belonging to the Bunyamwera serogroup).[19,20] Importantly, neither BUNV nor BATV, the parent viruses, are known to cause hemorrhagic fever in humans. A similar situation is being observed now in North America, where new reassortant strains of Cache Valley virus, also from the Bunyamwera serogroup, have emerged with

altered properties.[21,22] The reassortment potential is high among OBVs belonging to the same serogroup, some of which contain members with different host tropism (for instance, OROV and SBV in the Simbu serogroup), raising the possibility of emergence of novel viruses with unpredictable properties.[23] Indeed, new pathogenic OBVs infecting humans or animals continue to be discovered throughout the world,[24–29] but despite their epidemic potential and the concomitant threat to human health, they remain understudied.

OBVs enter host cells via receptor-mediated endocytosis.[30] Although a *bona fide* entry receptor has not been identified, certain attachment factors required for entry have been reported, such as cell surface glycosaminoglycans for AKAV and SBV[31,32] or C-type lectins for LACV.[33] Upon uptake by the cell, the acidic environment triggers fusion of the viral lipid envelope with the endosomal membrane, releasing the genomic RNP complexes into the cytoplasm for genome transcription and replication. Membrane fusion is mediated by the envelope glycoprotein Gc,[34,35] which makes a heterodimer with Gn. Gn/Gc heterodimerization is required for transport of Gc into the Golgi apparatus of the infected cell,[36,37] where virion assembly takes place by budding across the Golgi membrane.[38–40] The resulting particles display prominent spikes, with tripodal projections connected by a base or "floor" region parallel to the viral membrane.[41] The projections have been shown to be formed by the N-terminal half of Gc (Gc^S),[42] while the floor has been predicted to contain the C-terminal moiety (Gc^F) in complex with Gn.

Previous studies with BUNV had shown that the Gc^S portion is dispensable for virus entry, implying that OBV Gc^F is by itself fusion competent.[35] To provide mechanistic insight into OBV-driven membrane fusion, we here report the X-ray structures of LACV and SBV Gc^F in the post-fusion, trimer-of-hairpins conformation. This study unambiguously identified OBV Gc^F as a class II membrane fusion protein fused at its N terminus to the large Gc^S spike domain, unlike any other class II fusion protein described to date. Structure-guided mutagenesis yielded functional evidence for a key role of a vestigial endoplasmic reticulum (ER) translocation signal sequence at the Gc^S-Gc^F boundary, which provides intra-protomer stabilizing contacts to the post-fusion Gc^F trimer. The structures also revealed a tri-partite host membrane insertion surface (HMIS) at the trimer tip, and targeted mutagenesis confirmed the functional importance of non-polar residues exposed by the three loops of the HMIS for membrane fusion activity. The structures further revealed key conserved intra- and inter-protomer interactions stabilizing the post-fusion hairpin and its trimeric contacts, providing high-resolution snapshots of a fundamental step of the viral life cycle. We anticipate that our structural analysis will support the development of therapeutic biologicals for future treatment of OBV diseases.

RESULTS

OBV Gc^F constructs and X-ray structure determination

OBV Gc^F has been predicted to fold as a class II fusion protein,[34,43] homologous to its flavivirus[44] and alphavirus[45] counterparts, despite the absence of significant amino acid sequence identity. Similar predictions have been made for the fusion proteins of members of other families in the *Bunyavirales* order, which were later confirmed experimentally.[46–51] The amino acid sequence identity between OBV Gc^F and Gc from viruses in other families of the *Bunyavirales* order is very low, under 12%, whereas the amino acid (aa) sequence identity of LACV Gc^F with its orthologs within the OBV genus is between 40% and 70%.

The "class II" fold displays three characteristic structured domains (DI, DII, and DIII), followed by an extended "stem" region preceding the C-terminal transmembrane (TM) segment, as illustrated schematically in Figure 1A. With ~40% aa sequence identity, LACV and SBV Gc^F are among the most distant orthologs within the OBV genus. Based on secondary structure predictions and structural comparisons, we prepared constructs for expression of a soluble version of LACV Gc^F (LACV Gc 918–1,364, lacking the TM segment) and SBV Gc^F (fragment SBV Gc 881–1,306, lacking the TM region and the stem). Whereas the wild-type SBV Gc 881–1,306 construct yielded diffraction-quality crystals, the LACV construct required the single point mutation W1066H in the predicted *cd* fusion loop[52] to form trimers that crystallize (Figure S1). We determined the X-ray structures of the soluble SBV and LACV Gc^F constructs to 1.85 Å and 3.16 Å resolution, respectively, as described in STAR Methods (see Table 1 for the crystallography statistics).

The OBV Gc^F post-fusion trimer

The structures of the LACV and SBV Gc^F showed the canonical organization of class II membrane fusion proteins in their characteristic trimer-of-hairpins post-fusion conformation (Figures 1B and 1C). The inner arm of the post-fusion hairpin is composed of DI and DII (red and yellow, respectively, in Figure 1), which form an elongated rod, with the distal tip of DII projecting three loops (labeled *bc*, *cd*, and *ij* in Figures 1B and 1C). As discussed below, these loops expose non-polar side chains that insert into the target membrane to drive its fusion with the viral envelope (Figure 1A). They are therefore termed "fusion loops" and make up the HMIS defined above. The hairpin's outer arm is formed by the DI/DIII linker (cyan), DIII (blue), and the stem (magenta, absent in the SBV Gc^F construct). The hairpin's inner arms make contacts along their entire length to make a trimeric core, with tighter contacts at the tip and at the base, also corresponding to conserved regions of the molecule (Figures 2A and 2B, bottom panels). The outer arm packs at the periphery of the core trimer, interacting all along the core trimer interface, further stabilizing the post-fusion trimer (Figure 2C). Although LACV Gc^F crystallized at pH 8 and SBV Gc^F at pH 5.5, the two core trimer structures are highly similar, with the DI/DII portions aligning with a root-mean-square deviation (RMSD) of 0.7 Å (272 Cα atoms) and 0.8 Å (795 Cα atoms) for protomer and trimer, respectively. DIII aligns with 0.6 Å RMSD (56 Cα atoms), and upon alignment of the core trimers, it is shifted by 5–7 Å between the two structures in a plane normal to the molecular 3-fold axis, resulting in a slightly different quaternary arrangement of the Gc^F trimer. This shift could be caused by the absence of the stem in the SBV Gc^F structure.

In the trimer of hairpins, the DI/DIII linker makes intra-chain interactions only, adding an extra β strand (J_0) to the DI outer β sheet (Figures 1B and 1C). DIII packs at the level of the DI/DII

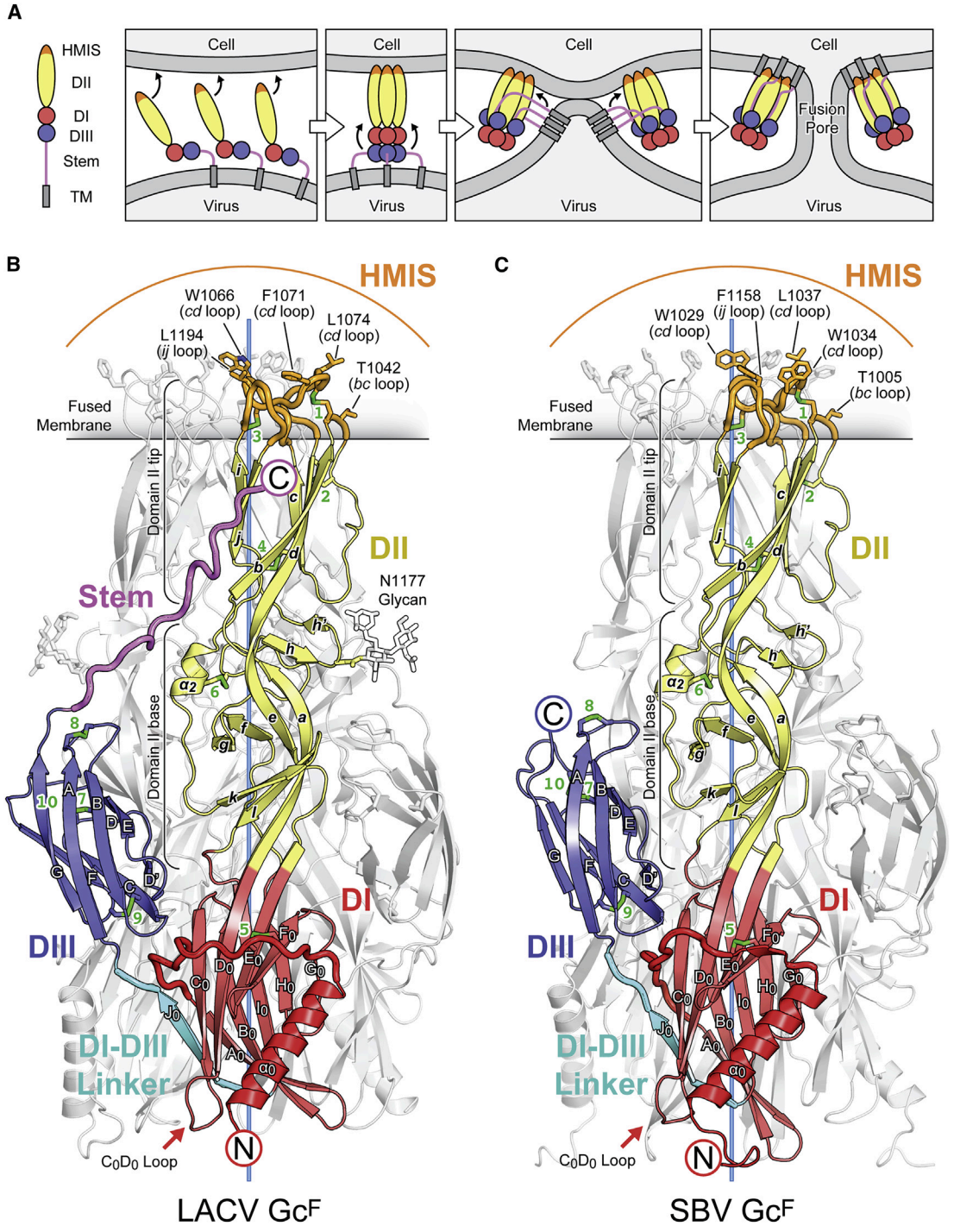

Figure 1. OBV Gc^F displays a class II fusion protein fold

(A) Schematic showing the domain composition of class II fusion proteins and the mechanism they use to drive membrane fusion.

(B) Structure of the LACV Gc^F post-fusion trimer.

(C) Structure of the SBV Gc^F post-fusion trimer. In (B) and (C), the front protomer is colored according to domains and the remaining two protomers of the trimer in light gray. A vertical light blue bar indicates the trimer axis. Secondary structure elements are labeled, and disulfide bonds are shown as sticks and numbered in green. The N and C termini are indicated within a colored circle. The red arrow points to antigenic site 7 (mapping to the C_0D_0 loop) described in the text.

Table 1. Crystallographic data collection and refinement statistics

	SBV Gc(881–1,306)	LACV Gc(918–1,364)
PDB ID	7a56	7a57
Reservoir solution for crystallization	20% (w/v) polyethylene glycol 1K, 0.1 M Na/K phosphate (pH 6.2), 0.2 M NaCl	0.1 M Bis-Tris propane (pH 7), 1.2 M K/Na tartrate (final pH: 8.0)
Data collection and processing[a]		
Beamline	ID23-2/European Synchrotron Radiation Facility (ESRF)	PX1/Synchrotron SOLEIL
Detector	PILATUS3 X 2M	PILATUS 6M
Wavelength (Å)	0.8729	0.9786
Space group	*H* 3 2	*P* 6_1 2 2
Unit cell *a*, *b*, *c* (Å) α, β, γ (°)	 86.79, 86.79, 358.09 90, 90, 120	 170.87, 170.87, 379.22 90, 90, 120
Resolution range[a] (Å)	43.40–1.85 (1.89–1.85)	48.17–3.16 (3.49–3.16)
Ellipsoidal resolution (Å)/direction	1.85/*a** 1.85/*b** 1.85/*c**	3.85/0.894 *a**–0.447 *b** 3.85/*b** 3.09/*c**
Unique reflections[b]	44,638 (2,661)	38,252 (1,913)
Completeness, spherical[b] (%)	99.5 (99.1)	67.1 (13.3)
Completeness, ellipsoidal[b,c] (%)	99.5 (99.1)	94.1 (74.8)
Redundancy[a]	6.2 (6.5)	6.3 (6.0)
R_{sym}[b]	0.108 (1.225)	0.132 (1.076)
R_{meas}[b]	0.118 (1.330)	0.144 (1.177)
R_{pim}[b]	0.047 (0.516)	0.057 (0.470)
$\langle I/\sigma(I)\rangle$[b]	9.5 (1.7)	9.2 (1.8)
$CC_{1/2}$[b]	0.997 (0.807)	0.998 (0.717)
Wilson *B*-factor (Å^2)	27.2	99.6
Structure refinement[d]		
Resolution range[b] (Å)	40.78–1.85 (1.92–1.85)	43.71–3.16 (3.27–3.16)
Unique reflections[b]	44,577 (4,344)	38,237 (157)
R_{work}[b]	0.17 (0.27)	0.20 (0.46)
R_{free}[b]	0.21 (0.29)	0.23 (0.27)
Number of atoms Protein Ligands/ions Water	3,673 3,228 26 419	10,385 10,271 114 –
Average *B*-factor (Å^2) Protein Ligands/ions Water	40.8 39.9 65.2 45.9	109.6 109.2 147.5 –
RMSD Bond lengths (Å) Bond angles (°)	 0.016 1.36	 0.005 0.91
Ramachandran distribution (%) favored Allowed Outliers	 96.39 3.37 0.24	 98.02 1.98 0.00
Number of TLS groups	2	6

[a]Processing statistics from Aimless.[53]
[b]Values in parentheses are for the highest-resolution shell.
[c]See STAR Methods for information on the anisotropic resolution cutoff applied.
[d]Refinement statistics from Phenix.[54]

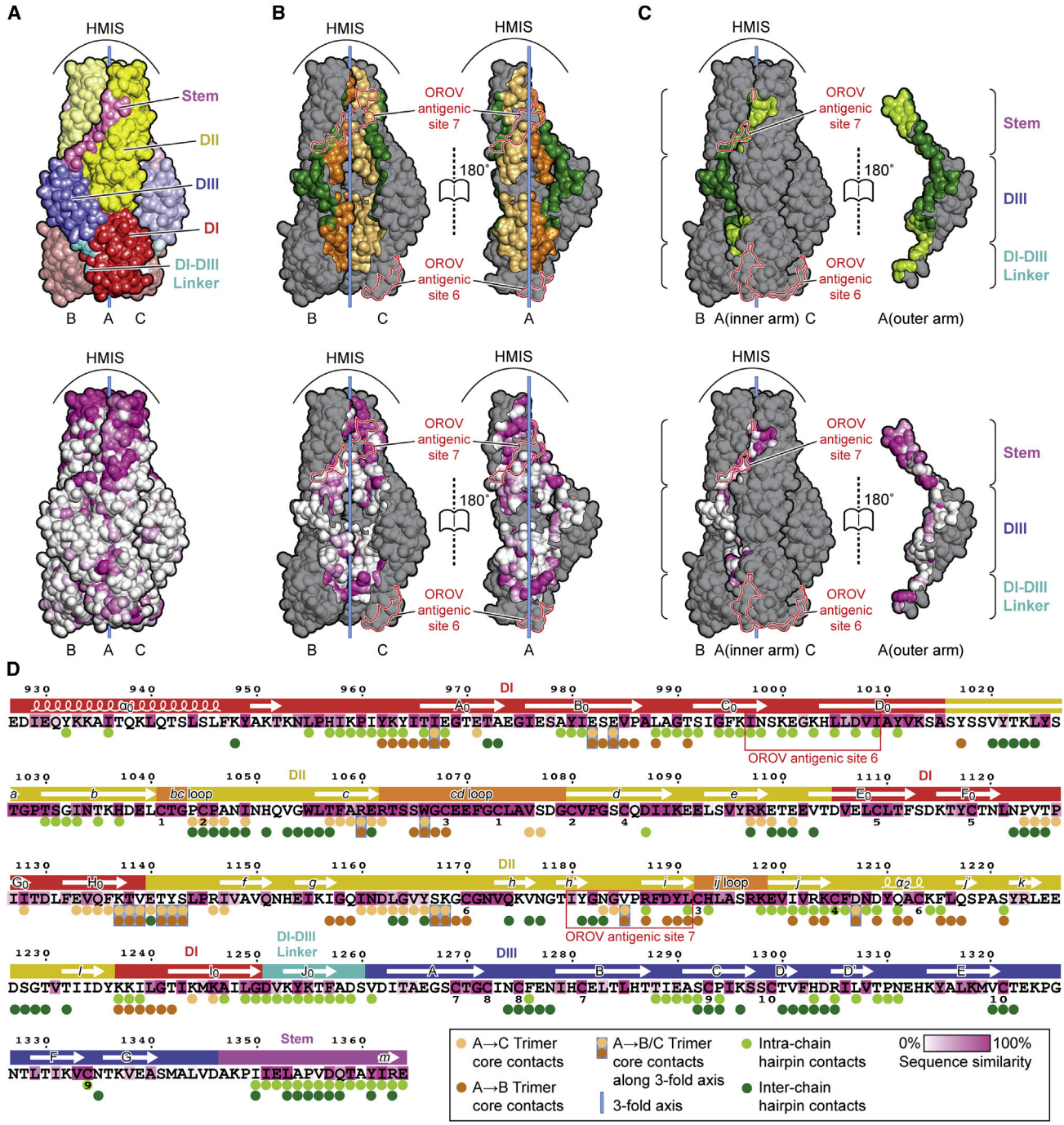

Figure 2. Trimer interface of post-fusion OBV Gc^F

(A) Solvent-accessible surface representation of LACV Gc^F colored by domains (top) or by sequence conservation across OBVs (below).

(B) Open-book representation with the front protomer (chain A) detached, colored by interface (top; see below for color key) or by sequence conservation (bottom panels). Two antigenic sites in OROV are outlined in red[55] (compare with Figures 1B, 1C, and S2). The trimer axis is displayed.

(C) Open-book representation with the outer arm (DI-DIII linker, DIII, and stem) of chain A detached.

(D) Sequence of LACV Gc^F color-coded by domain (top) and by sequence conservation across OBVs (highlight). Residue contribution to interfaces is indicated by dots below the sequence, colored-coded as in (B) and (C), top (see key in the bottom right inset, which applies to the entire figure). Note that the residues by the trimer axis have two dots, bright and light orange, as they make contacts with the two other chains. The sequence similarity across representative OBV species is plotted in shades of magenta.

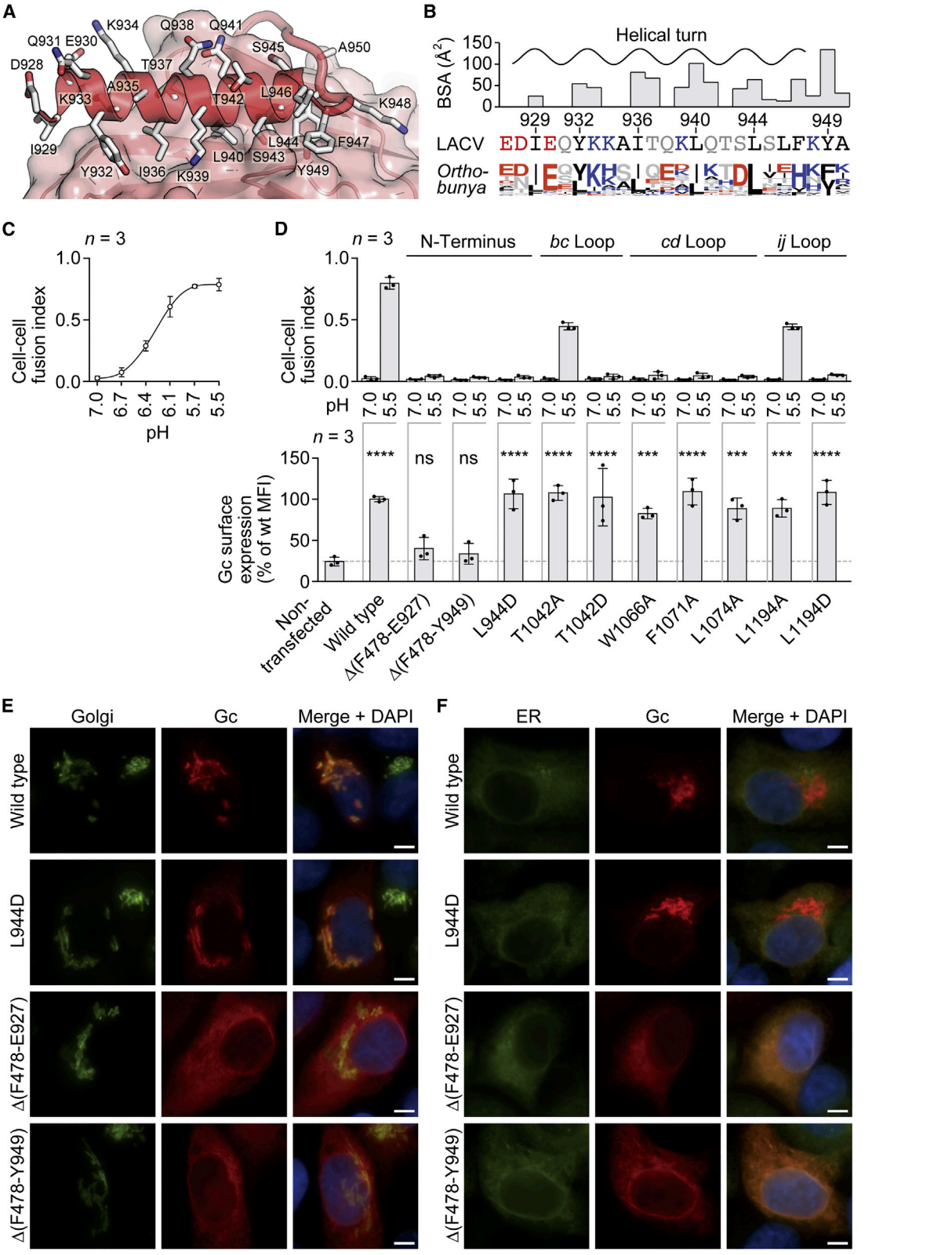

(legend on next page)

junction and makes intra- and inter-protomer contacts with DI and DII, respectively, while the stem aligns with DII in an extended conformation to reach the trimer tip. The stem also makes intra- and inter-chain contacts, but only the surfaces involved in intra-protomer interactions are highly conserved (Figure 2C), suggesting that hairpin formation is a built-in capacity of the individual polypeptide chains. Furthermore, the conserved interaction surfaces cluster at both ends of the outer arm (the stem's C-terminal end and at the DI/DIII linker), in line with the pattern of conservation of the interactions stabilizing the core trimer at the tip and at the base.

Of the 22 strictly conserved cysteine residues of the Gc^F ectodomain, 20 are visible in the electron density map, making 10 disulfide bonds (labeled in green in Figures 1B and 1C). The structures suggest that the last pair of conserved cysteines (absent in our crystallized constructs), would make an 11th disulfide bond positioned at the level of the HMIS, reaching the fused membrane upon full hairpin formation. C-terminal to the 11th disulfide, a segment of about 20 residues leads to the TM region, likely forming an amphipathic helix in the membrane-proximal external region (MPER), lying parallel to the membrane (Figure S2).

LACV Gc^F carries a single N-linked glycan in DII at position N1177 (*hh'* loop; Figures 1B and 2D), which contacts the stem of a neighboring protomer at position I1350 (Figure 1B). This glycosylation site is conserved in BUNV, where it was found to contribute to infection efficiency,[56] and in OROV (Figure S2), but not in SBV, despite its classification in the same serogroup as OROV.

Impact of Gc^S and helix α_0 on transport of the Gn/Gc complex to the cell surface and on Gc-driven syncytium formation at low pH

Having determined these structures, we set out to test the relevance of their most conspicuous features to the fusogenic activity of the OBV fusion machinery. Unique to OBV Gc is the presence of Gc^S connected to Gc^F via the N-terminal 5-turn helix α_0, which, in the post-fusion form, is tucked between the DI outer and inner β sheets, shielding the hydrophobic core of the DI β sandwich from contact with solvent (Figures 1B, 1C, 3A, and 3B). As discussed below, no similar helix is observed at this location in any other class II membrane fusion protein described so far. We set up a cell-cell fusion assay driven by the LACV glycoproteins to explore the importance of Gc^S and helix α_0 residues interacting with the DI hydrophobic core. The fusion assay involved overexpressing the intact LACV polyprotein precursor (i.e., the complete M segment open reading frame) in RK-13 cells to direct the fusion machinery to the plasma membrane and then exposing the cells to acidic pH to induce syncytium formation. Consistent with previous observations,[57] we found that the wild-type complex triggered efficient cell-cell fusion at pH 6.4 and reached its highest activity at pH 5.5 (Figure 3C).

Earlier studies on BUNV had shown that its Gc ortholog can tolerate a deletion comprising the entire Gc^S plus the first 10 residues of helix α_0[35]. We introduced similar deletions in LACV and found that constructs lacking either Gc^S alone or Gc^S and helix α_0 (mutants ΔF478-E927 and ΔF478-Y949, respectively) had lost syncytium formation activity (Figure 3D). Further experiments showed that neither of these two mutants trafficked to the cell surface, contrary to the wild-type protein (Figures 3D and S3), explaining the lack of activity. These results indicate that the presence of Gc^S is important for the proper conformation of the Gn/Gc complex and its transport out of the ER. Indeed, immunofluorescence experiments showed a diffuse intracellular localization consistent with aberrant retention in the ER, whereas the wild-type construct accumulated in the Golgi apparatus (Figures 3E and 3F) and could be detected at the cell surface (Figure S3). We thus conclude that, unlike the BUNV fusion machinery, its LACV counterpart critically relies on the presence of the Gc^S portion for its correct assembly.

Inspection of the structure showed that the conserved side chains of I936, L940, and L944, which project from three consecutive turns of helix α_0, insert tightly into the DI hydrophobic core (Figures 3A and 3B). We surmised that changing any of these three residues to aspartic acid would strongly affect the packing of the helix on the DI core because a negative charge would be unstable within a hydrophobic environment. We therefore prepared mutant L944D in the context of the full M segment open reading frame. This mutant showed normal cell surface expression and intracellular localization, but unlike wild-type Gc, it failed to induce syncytium formation upon acidification of transfected cells (Figures 3D–3F and S3). We conclude that the stabilizing interaction of helix α_0 with the hydrophobic core of DI is important for OBV fusion activity.

Taken together, these experiments show that, in the context of the LACV M segment, which also encodes proteins Gn and NSm (Figure 4B), a construct having a suboptimal interaction between helix α_0 and the DI core results in a Gn/Gc complex that reaches the cell surface, but in a form that is non-functional for driving syncytium formation. In contrast, the LACV constructs lacking the Gc^S moiety resulted in a Gn/Gc^F complex that did not reach the cell surface, despite mutant ΔF478-E927 still containing the entire helix α_0. Because heterodimerization with Gn is essential for transport of Gc out of the ER,[36,37] this observation suggests

Figure 3. Functional assessment of residues in helix α_0 and in the HMIS

(A) Structure of the LACV Gc helix α_0 on the surface of DI.

(B) Buried surface area (BSA) per residue over the sequence of LACV Gc helix α_0. The helical turn is indicated by a sine curve. The consensus sequence logo for the OBV genus is shown below. The residue type is color coded: non-polar (black), acidic (red), and basic (blue).

(C) pH dependency of wild-type LACV Gc-induced syncytium formation of RK-13 cells.

(D) Syncytium formation of RK-13 cells expressing LACV wild-type or mutant glycoproteins at pH 5.5 compared with pH 7.0 (top) and cell surface expression of LACV wild-type or mutant Gc as determined by immunofluorescence compared with non-transfected cells (see also Figure S3). Statistical analysis was performed using Dunnett's test with $\alpha = 0.05$. ****$p < 0.0001$; ***$p < 0.001$; ns (not significant), $p > 0.05$. All data are represented as means ± SD.

(E) Co-staining of the Golgi apparatus (green) and LACV Gc (red) on RK-13 cells expressing wild-type or mutant glycoproteins.

(F) Co-staining of ER (green) and LACV Gc (red) on RK-13 cells expressing wild-type or mutant glycoproteins.

Scale bars, 5 μm.

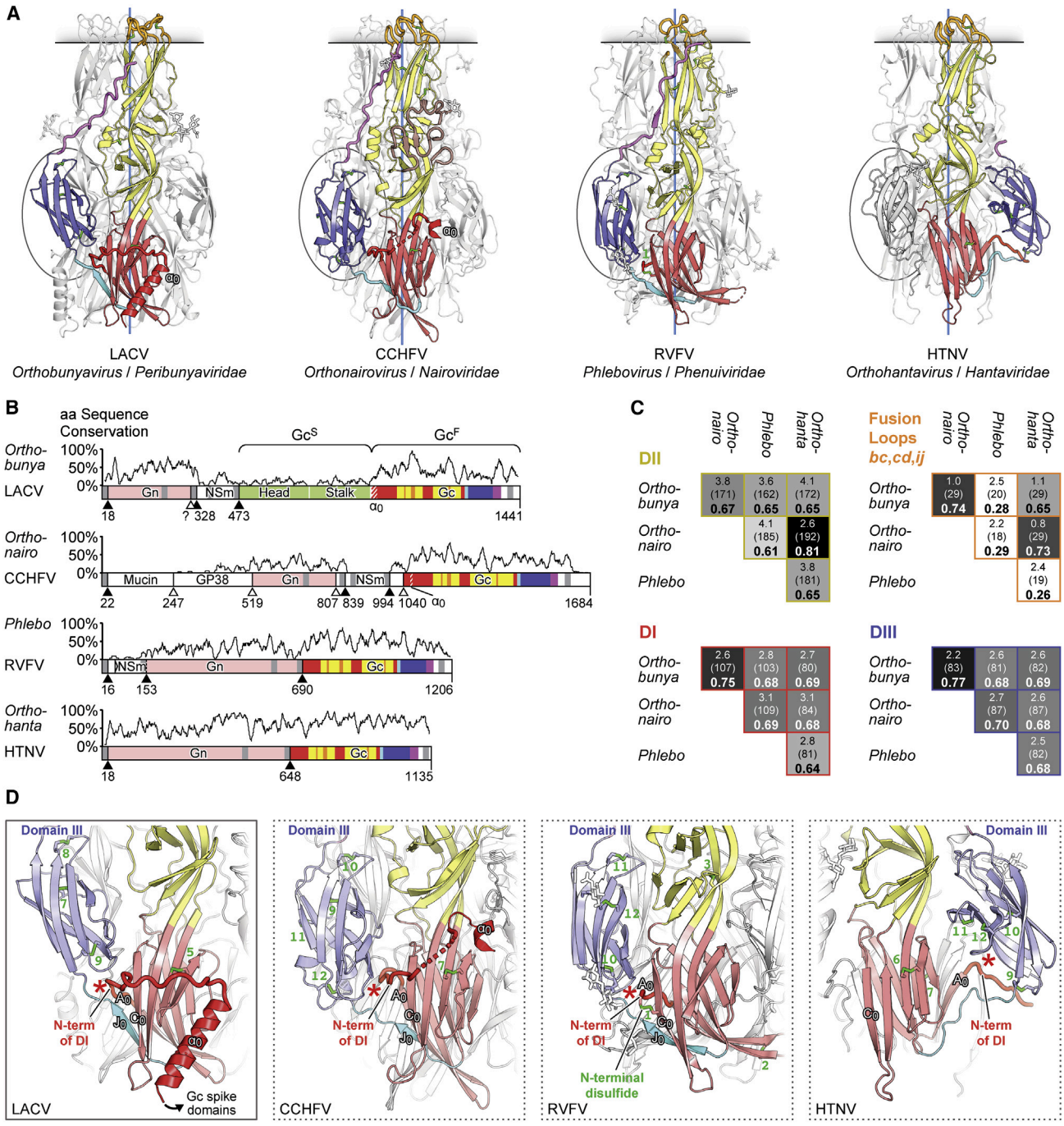

Figure 4. Comparison of OBV Gc^F with its orthologs from other zoonotic bunyaviruses

(A) Post-fusion trimer structures of LACV Gc^F shown next to Gc from the Crimean-Congo hemorrhagic fever virus (CCHFV),[50] Rift Valley fever virus (RVFV),[47] and the Hantaan hantavirus (HTNV).[48] The canonical location of domain III in the post-fusion trimer is highlighted within an ellipse. See also Figure S4 for a sequence alignment.

(B) Linear diagrams of the polyprotein precursor encoded in the M segment of viruses in the OBV, *Orthonairovirus*, *Orthohantavirus*, and *Phlebovirus* genera. The local sequence similarity across representative species from each genus is plotted over the diagrams. Putative TM helices are displayed in gray, signal peptidase cleavage sites are indicated by full triangles, and cleavage sites for other host proteases are indicated by empty triangles. Gn is shown in light red, OBV Gc^S in green, and Gc^F is colored by domains. All four diagrams are at the same scale (aa/cm).

(legend continued on next page)

that the presence of Gc^S is important for correct heterodimerization with Gn in the case of LACV, even though it was not required for BUNV.[35] A likely explanation for this discrepancy is that the aa sequence identity in the M segment (40% for the most conserved Gc^F portion, implying that 60% of the amino acids are different), is responsible for the observed differences. The AlphaFold prediction of the pre-fusion Gn/Gc complex recently reported[58] indeed showed that not only Gc^F interacts with Gn in the heterodimer but also the second subdomain of the stalk region of Gc^S (Figure 4B). This interaction appears to be dispensable for BUNV but not for LACV, in line with data from Plassmeyer et al.[34] showing that the C-terminal two-thirds of LACV Gc were required (aas 860–1,442, including most of the second stalk subdomain in Gc^S; Figure 4B) instead of one-half of BUNV Gc, as shown by Shi et al.[35]

Functional tests of the HMIS

Another salient feature of Gc^F is the high conservation of the HMIS (Figure 2A, bottom panel). In the initial steps of membrane fusion, the non-polar side chains projecting from the HMIS are known to interact with the aliphatic tails of lipids in the outer leaflet of the target membrane (as outlined in Figure 1A). We used the cell-cell fusion assay described above to test alanine substitutions W1066A, F1071A, and L1074A at the tip of the LACV *cd* loop. Assayed individually, each one of these mutations strongly impaired pH-dependent fusion, indicating a firm requirement for each of these large non-polar side chains for insertion into the outer leaflet of the target membrane (Figure 3D). Among these substitutions, only the L1074A mutation can be found in a natural OBV, Nyando virus, where it is likely compensated by the nearby G1072M mutation (LACV numbering; Figure S2). In contrast to the *cd* loop, the tips of the two flanking loops of the HMIS did tolerate alanine substitutions; the hydrophilic T1042 side chain on the *bc* loop is strictly conserved across the OBV genus, but its alanine substitution mutant retained fusion activity in our assay (Figure 3D). We observed a similar phenotype with the L1194A substitution at the tip of the *ij* loop, and indeed, alanine is frequently observed at this position in natural viruses (Figure S2). In contrast, syncytium formation was abrogated by the T1042D or L1194D substitution (Figure 3D), demonstrating incompatibility between the presence of a negative charge within this surface and its insertion into the outer leaflet of the membrane. The controls showed that all Gn/Gc heterodimers with HMIS point mutations were expressed to similar levels on the cell surface (Figures 3D, bottom panel, and S3).

Comparison with Gc from other families of zoonotic bunyaviruses

Five of the 14 virus families currently classified within the *Bunyavirales* order (https://ictv.global/taxonomy) contain zoonotic human pathogenic viruses, two of them encompassing viruses that persistently infect rodents and cause spillover disease in humans (*Arenaviridae* and *Hantaviridae* families; notable members are Lassa fever virus and Sin Nombre virus, respectively). The other three families contain arboviruses: the *Phenuiviridae*, *Nairoviridae*, and *Peribunyaviridae* families, with the most studied species among them being the Rift Valley fever virus (RVFV), the Crimean-Congo hemorrhagic fever virus (CCHFV), and LACV, respectively. Except for the viruses in the *Arenaviridae* family, which have a class I fusion protein,[60,61] all others have a class II fusion machinery composed of a heterodimer of glycoproteins Gn and Gc.[62]

The Gc post-fusion trimers of representative viruses from each of these four families are displayed in Figure 4A with the organization of their M segment, coding for the precursor of Gn and Gc, shown in Figure 4B. Because of the poor conservation of the Gc aa sequence across them, we superposed the atomic models displayed in Figure 4A, which led to the structural alignment presented in Figure S4. To investigate the structural similarity domain-wise, we used the "template modeling score,"[59] which provides an absolute number that is comparable across domains because it does not depend on the domain size, unlike the RMSD value. This analysis showed that, although the three domains display the same 3D structure (template modeling score > 0.6), in the Phenuiviridae, the fusion loops are different (Figure 4C). It also showed that, although DI and DIII are most similar between OBV and the nairovirus counterpart, for DII the highest score is between hantaviruses and nairoviruses (Figure 4C).

The DI/DIII linker

We tested the accuracy of structural predictions for the LACV Gc^F post-fusion trimer using AlphaFold Multimer,[63] which provided a very good model for the core trimer formed by the hairpin's inner arm, but the predictions for the outer arm were substantially off (Figure S5A). We note that the DI-DIII linker in the AlphaFold prediction is in a conformation very similar to that observed in Gc orthologs crystallized in a pre-fusion form (Figures S5C and S5D), in line with a convincing AlphaFold prediction of prefusion BUNV Gn/Gc heterodimer structure reported recently.[58] The high number of available aa sequences for Gc from OBVs and from viruses of other genera in the *Peribunyaviridae* family have very likely contributed to the accuracy of the AlphaFold prediction of the pre-fusion form. However, the function of Gc, which must adopt different conformations at different stages of the virus cycle, still poses a challenge for artificial-intelligence-based structure prediction methods to sort out relevant, stage-dependent intra- and inter-protomer interactions. The J_0 strand, formed by the DI/DIII linker (Figures 1B, 1C, and 4D, left panel, cyan) running antiparallel to the C_0 strand of DI, directs DIII into its location in the post-fusion hairpin. This strand is not present in the available pre-fusion structures of other class II

(C) Cα atom root-mean-square deviation (RMSD) and template modeling score[59] upon pairwise 3D superposition of the Gc individual domains, as indicated (including the fusion loops as outlined in Figure 5A, although they do not constitute a separate domain). The number of Cα atom pairs of each domain used in the superposition is provided in parentheses.

(D) Close ups of the DI-DIII linker and its interaction in post-fusion Gc of representative members of the OBV, *Orthonairovirus*, *Orthohantavirus*, and *Phlebovirus* genera. The N-terminal segment of DI is labeled, and its interaction site with DIII is indicated by an asterisk in each structure. The red dotted line in the second panel denotes a disordered segment.

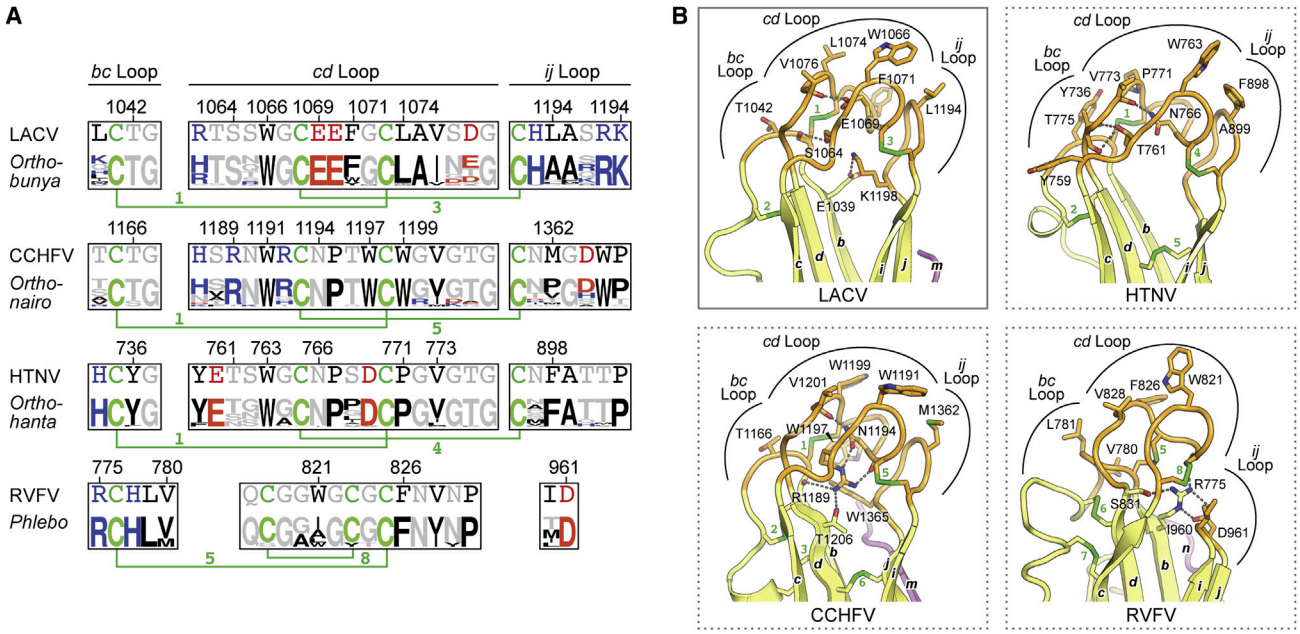

Figure 5. The host membrane insertion surface (HMIS)

(A) Fusion loop sequences of Gc from the four genera analyzed in Figure 4 with the consensus sequence logo of the corresponding viral genus, as indicated. The residue type is color coded: non-polar (black), acidic (red), basic (blue), and disulfides (green).

(B) Conformations of the fusion loops in post-fusion LACV Gc, CCHFV Gc,[50] HTNV Gc,[48] and RVFV Gc.[47] DII is shown as yellow ribbons with the HMIS in orange and relevant side chains as sticks. Note that in RVFV, the *ij* loop is colored orange, although it is not part of the HMIS.

fusion proteins (see Figures S5B and S5C for the closest examples) and is not predicted by AlphaFold (compare the top and center panels of Figure S5A). Furthermore, the Gc N-terminal tail immediately upstream of the A_0 strand of DI (marked with a red star in Figure 4D) stabilizes DIII in its post-fusion location, as also observed in the nairovirus Gc post-fusion structure (Figure 4D, second panel; see also Figure S5C). The correct packing of helix α_0 farther upstream on the N-terminal tail appears to be required for maintaining the structure supporting DIII, as shown by the functional data with the L944D mutant (Figure 2B). In the case of phlebovirus Gc, this support role is taken up by a conserved N-terminal disulfide bond (Figure 4D, third panel; see also Figure S5B). Failure to predict these two essential secondary structure elements of the post-fusion hairpin, β strand J_0 and helix α_0, by AlphaFold propagates also into misprediction of the DIII location in the post-fusion form (Figure S5A).

In contrast to the similar arrangement of DIII in the arthropod-borne bunyaviruses, hantavirus Gc DIII is swapped among neighboring protomers of the post-fusion trimers[48,51] (Figures 4A and 4D, right panels). However, DIII from the adjacent protomer makes inter-protomer interactions essentially identical to the intra-protomer ones (and vice versa) observed in Gc from the arboviruses (circled in the four structures displayed in Figure 4A). The domain swap results in an altogether different conformation of the DI-DIII linker, which makes a very different set of interactions (Figure 4D, compare the fourth panel with the other three). There is no J_0 strand, and the Gc N-terminal tail follows the DI/DIII linker to pack against the adjacent protomer, complementing its DI with an additional A_0 strand and making inter-chain β interactions not present in the pre-fusion form[48,64] (Figure 4D, right panel). An analogous swapping of DIII was also observed in the post-fusion trimer of Rubella virus glycoprotein E1,[65] the only other non-arbovirus class II fusion protein of known structure.

Comparison of the HMISs

The HMIS is the most conserved region of Gc^F within the OBV genus (Figure 2A, bottom panel). This conservation is lost when comparing across the bunyavirus families (Figure 5A), although the three loops composing the HMIS have the same lengths and the same disulfide bonding pattern in Gc from viruses of three of the four families analyzed, which also share a conserved tryptophan at the same location in the *cd* loop (Figures 5A, top three rows, and 5B, first three panels). In the *Phenuiviridae*, the fusion loops are different (Figure 4C); the *ij* loop does not reach the DII tip (Figure 5B, last panel), and the HMIS is formed by the *bc* and *cd* loops only but maintains the disulfide bond connecting the two loops (Figures 5A, fourth row, and 5B; disulfide bond numbered 5 in RVFV and 1 in the others). The *cd* loop makes the largest contribution to the HMIS in all class II fusion proteins. For hantavirus Gc, residues in the *bc* and *ij* loops have been shown experimentally to also be essential for insertion into target membranes and for Gc-driven membrane fusion.[48] The equivalent residues in nairovirus Gc have been tested recently and shown to also be functionally required,[50] and we confirm here that this is also the case for OBV Gc (Figure 2D).

The topology of the OBV HMIS is stabilized by the conserved disulfide bonds 1, 2, and 3 (green in Figure 5), which are conserved in hantavirus and nairovirus Gc (Figures 5B and S4).

The HMIS is further supported by hydrogen bonds involving the buried polar S1064 and E1069 side chains of the *cd* loop (LACV numbering; Figure 5B). The corresponding residues in hantavirus Gc, N764 and N769, are also buried and engage in similar interactions in the post-fusion form but are surface exposed at the DII tip in the X-ray structure of the pre-fusion hantavirus Gn/Gc heterodimer.[64] Furthermore, the non-polar side chains exposed at the HMIS were found to be either buried, such as hantavirus W766 (Maporal hantavirus numbering), corresponding to LACV W1066, or at the interface with Gn in the pre-fusion form. Liposome interaction assays with hantavirus particles have suggested that these conformational changes in the fusion loops are reversible and that the equilibrium between the two states, exposed and Gn cloaked, is temperature dependent, with higher temperatures favoring the active conformation in which the HMIS is formed by exposure of non-polar side chains.[66] As proposed for nairoviruses,[50] we postulate that a conformational change akin to the one observed in hantavirus Gc may take place in OBVs upon Gn/Gc heterodimer dissociation at the endosomal pH. The polar side chains of LACV Gc S1064 and E1069 observed to be buried at the DII tip would likewise be exposed to the surface in the pre-fusion Gn/Gc complex, a postulate that remains to be experimentally confirmed. We thus conclude that the HMIS of OBV, nairovirus, and hantavirus Gc are not only structurally conserved (Figure 4C) but that their essential fusion determinants are also distributed similarly over the three fusion loops and function in a similar way.

DISCUSSION

The structures of LACV and SBV Gc^F fill an important gap because they belong to the only and largest group of human pathogenic bunyaviruses for which structural information on the fusion protein has been lacking. Previous experiments based on weak similarity with the alphavirus class II fusion glycoprotein E1 had concluded that the LACV Gc segment 1,066–1,087 was the "fusion loop."[52] This prediction was essentially correct because the *cd* loop (residues 1,062–1,079; Figure 5) is indeed the main component of the HMIS. The previous alanine scanning data on LACV had shown that mutant W1066A was unable to drive fusion, as we also experimentally confirm here. We also show that point mutants F1071A and L1074A, two other non-polar residues prominently exposed at the HMIS, also result in a fusion-incompetent protein.

One mutant tested in the reported alanine scanning, G1083A, has been shown to have a folding defect.[52] G1083 lies in the middle of β strand *d*, where the side chain of F1058 of the adjacent β strand *c* (also a strictly conserved residue across OBVs; Figures 2 and S2) makes a π interaction with the main chain at the 1,083-1,084 peptide bond, leaving no space for an additional methyl group at the Cα of the 1,083 position (Figure S6), explaining why the mutation is not tolerated. We further note that the previous studies on hantavirus Gc discussed above showed that this precise region of the DII tip is involved in the conformational change required for formation of the post-fusion HMIS upon dissociation from Gn.[48,64] This information thus offers a potential new target for antiviral compounds binding the hydrophobic core of the domain II tip and blocking formation of the HMIS. The strict conservation of the residues involved across the OBV genus suggests that development of resistance to such compounds without affecting viral fitness is unlikely. A high-resolution experimental structure of the pre-fusion OBV Gn/Gc heterodimer is not yet available, and the AlphaFold model predicts a Gn/Gc complex in which the DII tip has the HMIS as observed in the post-fusion form,[58] whereas it is expected to display an alternative conformation.

Mutants LACV Gc G1067A, V1076A, and D1078A in the *cd* loop have been reported to be only partially impaired in fusion.[52] Recombinant viruses with these point mutations have been rescued and shown to have an attenuated phenotype in cell culture[67] and *in vivo* experiments, where they were not neuroinvasive as the parent LACV.[68] The structure now shows that the side chain of T1042 in the *bc* loop, whose mutation to alanine also has a reduced fusion phenotype in our assay (Figure 2), hydrogen bonds the D1078 side chain tested in the previous study (Figure S6). The strict conservation of these two residues across OBVs (Figure S2) highlights the importance of this interaction.

This knowledge could be used for development of a live-attenuated vaccine against zoonotic viruses such as LACV, which could also be used to vaccinate wild animals constituting a potential reservoir, as was done to eradicate rabies in several European countries.[69,70] However, a live vaccine used in the wild would require genetic stability of the attenuated virus. Introducing several mutations on HMIS residues that contribute to an attenuated phenotype (for instance, simultaneously mutating T1042 and D1078) is one way to reduce the chances of reversion. A mutation less drastic than L988D in helix α_0 (for instance, L988A or L988T) (Figure 3), weakening its interactions with the hydrophobic core of DI, could also serve this purpose. A similar approach was used recently with the live-attenuated oral poliovirus vaccine, in which several mutations were introduced in the virus genome to limit the appearance of vaccine revertants with epidemic potential.[71] However, because the OBV genome is segmented and the probability of reassortment is high, all three segments would need to be engineered into an attenuated phenotype to mitigate the potential emergence of vaccine-derived virulent strains. Such an approach is feasible, especially because there are X-ray structures available for the S-segment-encoded nucleoprotein from LACV[12] and other OBVs[72] as well as X-ray and electron cryo-microscopy (cryo-EM) structural data for the L-segment-encoded LACV polymerase.[13] A concerted approach targeting proteins encoded by the three bunyavirus genomic segments could thus strongly limit the risk of reassortants emerging with a vaccine-derived genome segment.

The information provided by the Gc^F structures reported here can also be transposed to other OBVs; for instance, OROV, the most prevalent arbovirus after Dengue virus in Brazil[73,74] and elsewhere in South America.[75–77] A seroprevalence of 15%–30% in certain urban areas indicates that OROV infections are highly under-diagnosed.[78,79] A recent study, immunizing mice with vesicular stomatitis virus pseudotyped with the OROV glycoproteins, showed that deletion of parts of Gc^S led to a more protective immune response, with antibodies directed to Gc^F and Gn,[55] whereas normally the immune response is directed exclusively to Gc^S. Mapping the antibody-reactive peptides identified in that study to the OBV post-fusion structure identified

antigenic sites 6 and 7 (Figures 2 and S2). These sites involve surfaces of the Gc^F protomer that become occluded during post-fusion homotrimerization (site 7) or that must be flexible for post-fusion hairpin formation (site 6; this flexible segment is also indicated by the red arrow in Figures 1B and 1C). Similar antigenic sites were identified recently in the nairovirus CCHFV Gc[50] and in Puumala hantavirus Gc[80] as targets of potently neutralizing antibodies. Furthermore, serum from mice immunized with deletions in Gc^S neutralized authentic OROV, indicating that the floor of the OBV surface lattice[42,58] is accessible to circulating antibodies and that it is the high immunogenicity of the projecting spikes that results in an antibody response selective for Gc^S. These data suggest that immunization with a pre-fusion form of Gc^F (i.e., as a fusion-incompetent pseudotype lacking large portions of Gc^S or as a subunit vaccine consisting of a disulfide-locked Gn/Gc^F heterodimer) should elicit broadly protective antibodies, and our structure provides a rationale to identify their neutralization mechanism.

The comparative analyses with structures of Gc from more distant bunyaviruses shows how identical functional constraints are built in within a different aa sequence context, a testimony to the different evolutionary pathways taken by the individual viral families. The derived knowledge is highly valuable to infer mechanistic insight about Gc's function and for identifying ways to inactivate it. Our study also shows that experimental structure determination remains essential: the most advanced structure prediction program available today, AlphaFold2,[81] produced a plausible atomic model of the Gc pre-fusion form,[58] but with an incorrect prediction of the post-fusion hairpin (Figure S4A), highlighting the importance of independent experimental validation of the predicted structures.

Our structures of LACV and SBV Gc^F provide a wealth of detailed information on key conserved interactions required to drive the membrane fusion reaction for entry, an essential step for all enveloped viruses, that can be targeted for therapeutic and prophylactic approaches. Beyond LACV, the conserved sites can be used to derive specific antiviral agents to protect from a vast range of diseases caused by members of the large OBV genus.

Limitations of the study

The presented structures of Gc^F show only part of the entire Gc protein, and it still remains to be determined how Gc^S and the Gc TM region are arranged in the context of this post-fusion form. Additional experimental studies to determine a high-resolution structure of the pre-fusion Gn/Gc heterodimer are required to shed light on the postulated switch in conformation at the Gc tip to expose the HMIS only in the post-fusion form.

STAR★METHODS

Detailed methods are provided in the online version of this paper and include the following:

SUPPLEMENTAL INFORMATION

Supplemental information can be found online at https://doi.org/10.1016/j.celrep.2023.112142.

ACKNOWLEDGMENTS

This research was performed as part of the Zoonoses Anticipation and Preparedness Initiative (ZAPI project; IMI grant agreement 115760) with the assistance and financial support of IMI and the European Commission and in-kind contributions from EFPIA partners. Additional funding was provided by Institut Pasteur, CNRS, and grant ANR-10-LABX-62-IBEID (to F.A.R.). J.H. received the Pasteur-Cantarini fellowship for 24 months and was further supported by the Région Ile de France (Domaine d'intêret majeur innovative technologies for life sciences, DIM 1HEALTH). We thank the staff of the crystallography platform at Institut Pasteur for robot-driven crystallization screening. We also thank Fabrice Agou from the Chemogenomic and Biological Screening platform at Institut Pasteur and the staff of synchrotron beamlines PX1 at SOLEIL (St. Aubin, France) and ID23-2 at the ESRF (Grenoble, France) for help during data collection.

AUTHOR CONTRIBUTIONS

J.H., A.A., and F.A.R. designed the experiments. J.H. produced the recombinant proteins and performed the biophysical and crystallographic analysis, to which A.H. and P.G.-C. contributed. A.A. performed the cell-cell fusion assay. S.R. and A.A. prepared the monoclonal antibody. J.H. and F.A.R. wrote the manuscript with contributions from all authors.

DECLARATION OF INTERESTS

The authors declare no competing interests.

INCLUSION AND DIVERSITY

We support inclusive, diverse, and equitable conduct of research.

Received: October 22, 2022
Revised: December 29, 2022
Accepted: February 7, 2023
Published: February 22, 2023

REFERENCES

1. Stephens, P.R., Gottdenker, N., Schatz, A.M., Schmidt, J.P., and Drake, J.M. (2021). Characteristics of the 100 largest modern zoonotic disease

outbreaks. Phil. Trans. R. Soc. B. *376*, 20200535. https://doi.org/10.1098/rstb.2020.0535.

2. Elliott, R.M. (2014). Orthobunyaviruses: recent genetic and structural insights. Nat. Rev. Microbiol. *12*, 673–685. https://doi.org/10.1038/nrmicro3332.

3. Windhaber, S., Xin, Q., and Lozach, P.Y. (2021). Orthobunyaviruses: from virus binding to penetration into mammalian host cells. Viruses *13*. https://doi.org/10.3390/v13050872.

4. Vahey, G.M., Lindsey, N.P., Staples, J.E., and Hills, S.L. (2021). La Crosse virus disease in the United States, 2003-2019. Am. J. Trop. Med. Hyg. *105*, 807–812. https://doi.org/10.4269/ajtmh.21-0294.

5. McJunkin, J.E., de los Reyes, E.C., Irazuzta, J.E., Caceres, M.J., Khan, R.R., Minnich, L.L., Fu, K.D., Lovett, G.D., Tsai, T., and Thompson, A. (2001). La Crosse encephalitis in children. N. Engl. J. Med. *344*, 801–807. https://doi.org/10.1056/NEJM200103153441103.

6. Martins-Luna, J., Del Valle-Mendoza, J., Silva-Caso, W., Sandoval, I., Del Valle, L.J., Palomares-Reyes, C., Carrillo-Ng, H., Peña-Tuesta, I., and Aguilar-Luis, M.A. (2020). Oropouche infection a neglected arbovirus in patients with acute febrile illness from the Peruvian coast. BMC Res. Notes *13*, 67. https://doi.org/10.1186/s13104-020-4937-1.

7. Travassos da Rosa, J.F., de Souza, W.M., Pinheiro, F.d.P., Figueiredo, M.L., Cardoso, J.F., Acrani, G.O., and Nunes, M.R.T. (2017). Oropouche virus: clinical, epidemiological, and molecular aspects of a neglected orthobunyavirus. Am. J. Trop. Med. Hyg. *96*, 1019–1030. https://doi.org/10.4269/ajtmh.16-0672.

8. Bowen, M.D., Trappier, S.G., Sanchez, A.J., Meyer, R.F., Goldsmith, C.S., Zaki, S.R., Dunster, L.M., Peters, C.J., Ksiazek, T.G., and Nichol, S.T.; RVF Task Force (2001). A reassortant bunyavirus isolated from acute hemorrhagic fever cases in Kenya and Somalia. Virology *291*, 185–190. https://doi.org/10.1006/viro.2001.1201.

9. Cichon, N., Barry, Y., Stoek, F., Diambar, A., Ba, A., Ziegler, U., Rissmann, M., Schulz, J., Haki, M.L., Höper, D., et al. (2021). Co-Circulation of orthobunyaviruses and Rift Valley fever virus in Mauritania, 2015. Front. Microbiol. *12*, 766977. https://doi.org/10.3389/fmicb.2021.766977.

10. Beer, M., Conraths, F.J., and van der Poel, W.H.M. (2013). 'Schmallenberg virus'–a novel orthobunyavirus emerging in Europe. Epidemiol. Infect. *141*, 1–8. https://doi.org/10.1017/S0950268812002245.

11. Hopkins, F.R., Alvarez-Rodriguez, B., Heath, G.R., Panayi, K., Hover, S., Edwards, T.A., Barr, J.N., and Fontana, J. (2022). The native orthobunyavirus ribonucleoprotein possesses a helical architecture. mBio *13*, e0140522. https://doi.org/10.1128/mbio.01405-22.

12. Reguera, J., Malet, H., Weber, F., and Cusack, S. (2013). Structural basis for encapsidation of genomic RNA by La Crosse Orthobunyavirus nucleoprotein. Proc. Natl. Acad. Sci. USA *110*, 7246–7251. https://doi.org/10.1073/pnas.1302298110.

13. Gerlach, P., Malet, H., Cusack, S., and Reguera, J. (2015). Structural insights into bunyavirus replication and its regulation by the vRNA promoter. Cell *161*, 1267–1279. https://doi.org/10.1016/j.cell.2015.05.006.

14. Shi, X., Botting, C.H., Li, P., Niglas, M., Brennan, B., Shirran, S.L., Szemiel, A.M., and Elliott, R.M. (2016). Bunyamwera orthobunyavirus glycoprotein precursor is processed by cellular signal peptidase and signal peptide peptidase. Proc. Natl. Acad. Sci. USA *113*, 8825–8830. https://doi.org/10.1073/pnas.1603364113.

15. Shi, X., Kohl, A., Li, P., and Elliott, R.M. (2007). Role of the cytoplasmic tail domains of Bunyamwera orthobunyavirus glycoproteins Gn and Gc in virus assembly and morphogenesis. J. Virol. *81*, 10151–10160. https://doi.org/10.1128/JVI.00573-07.

16. McDonald, S.M., Nelson, M.I., Turner, P.E., and Patton, J.T. (2016). Reassortment in segmented RNA viruses: mechanisms and outcomes. Nat. Rev. Microbiol. *14*, 448–460. https://doi.org/10.1038/nrmicro.2016.46.

17. Steel, J., and Lowen, A.C. (2014). Influenza A virus reassortment. Curr. Top. Microbiol. Immunol. *385*, 377–401. https://doi.org/10.1007/82_2014_395.

18. Briese, T., Calisher, C.H., and Higgs, S. (2013). Viruses of the family Bunyaviridae: are all available isolates reassortants? Virology *446*, 207–216. https://doi.org/10.1016/j.virol.2013.07.030.

19. Briese, T., Bird, B., Kapoor, V., Nichol, S.T., and Lipkin, W.I. (2006). Batai and Ngari viruses: M segment reassortment and association with severe febrile disease outbreaks in East Africa. J. Virol. *80*, 5627–5630. https://doi.org/10.1128/JVI.02448-05.

20. Gerrard, S.R., Li, L., Barrett, A.D., and Nichol, S.T. (2004). Ngari virus is a Bunyamwera virus reassortant that can be associated with large outbreaks of hemorrhagic fever in Africa. J. Virol. *78*, 8922–8926. https://doi.org/10.1128/JVI.78.16.8922-8926.2004.

21. Baker, M., Hughes, H.R., Naqvi, S.H., Yates, K., Velez, J.O., McGuirk, S., Schroder, B., Lambert, A.J., Kosoy, O.I., Pue, H., et al. (2021). Reassortant Cache Valley virus associated with acute febrile, nonneurologic illness, Missouri. Clin. Infect. Dis. *73*, 1700–1702. https://doi.org/10.1093/cid/ciab175.

22. Dieme, C., Maffei, J.G., Diarra, M., Koetzner, C.A., Kuo, L., Ngo, K.A., Dupuis Ii, A.P., Zink, S.D., Backenson, P.B., Kramer, L.D., and Ciota, A.T. (2022). Aedes Albopictus and Cache Valley virus: a new threat for virus transmission in New York State. Emerg. Microb. Infect. *11*, 741–748. https://doi.org/10.1080/22221751.2022.2044733.

23. Tilston-Lunel, N.L., Shi, X., Elliott, R.M., and Acrani, G.O. (2017). The potential for reassortment between oropouche and Schmallenberg orthobunyaviruses. Viruses *9*. https://doi.org/10.3390/v9080220.

24. Al-Heeti, O., Wu, E.L., Ison, M.G., Saluja, R.K., Ramsey, G., Matkovic, E., Ha, K., Hall, S., Banach, B., Wilson, M.R., et al. (2023). Transfusion-transmitted Cache Valley virus infection in a kidney transplant recipient with meningoencephalitis. Clin. Infect. Dis. *76*, e1320–e1327. https://doi.org/10.1093/cid/ciac566.

25. Ciccone, E.J., Markmann, A.J., Srinivas, M.L., Levinson, K.J., Miller, M.B., van Duin, D., and Gay, C.L. (2022). Encephalitis caused by jamestown Canyon virus in a liver transplant patient. Open Forum Infect. Dis. *9*, ofac031. https://doi.org/10.1093/ofid/ofac031.

26. Edridge, A.W.D., Deijs, M., Namazzi, R., Cristella, C., Jebbink, M.F., Maurer, I., Kootstra, N.A., Buluma, L.R., van Woensel, J.B.M., de Jong, M.D., et al. (2019). Novel orthobunyavirus identified in the cerebrospinal fluid of a Ugandan child with severe encephalopathy. Clin. Infect. Dis. *68*, 139–142. https://doi.org/10.1093/cid/ciy486.

27. Pérot, P., Bielle, F., Bigot, T., Foulongne, V., Bolloré, K., Chrétien, D., Gil, P., Gutiérrez, S., L'Ambert, G., Mokhtari, K., et al. (2021). Identification of Umbre orthobunyavirus as a novel zoonotic virus responsible for lethal encephalitis in 2 French patients with hypogammaglobulinemia. Clin. Infect. Dis. *72*, 1701–1708. https://doi.org/10.1093/cid/ciaa308.

28. Rodriguez, C., Gricourt, G., Ndebi, M., Demontant, V., Poiteau, L., Burrel, S., Boutolleau, D., Woerther, P.L., Calvez, V., Stroer, S., and Pawlotsky, J.M. (2020). Fatal encephalitis caused by cristoli virus, an emerging orthobunyavirus, France. Emerg. Infect. Dis. *26*, 1287–1290. https://doi.org/10.3201/eid2606.191431.

29. Wilson, M.R., Suan, D., Duggins, A., Schubert, R.D., Khan, L.M., Sample, H.A., Zorn, K.C., Rodrigues Hoffman, A., Blick, A., Shingde, M., and DeRisi, J.L. (2017). A novel cause of chronic viral meningoencephalitis: Cache Valley virus. Ann. Neurol. *82*, 105–114. https://doi.org/10.1002/ana.24982.

30. Hollidge, B.S., Nedelsky, N.B., Salzano, M.V., Fraser, J.W., González-Scarano, F., and Soldan, S.S. (2012). Orthobunyavirus entry into neurons and other mammalian cells occurs via clathrin-mediated endocytosis and requires trafficking into early endosomes. J. Virol. *86*, 7988–8001. https://doi.org/10.1128/JVI.00140-12.

31. Murakami, S., Takenaka-Uema, A., Kobayashi, T., Kato, K., Shimojima, M., Palmarini, M., and Horimoto, T. (2017). Heparan sulfate proteoglycan is an important attachment factor for cell entry of Akabane and Schmallenberg viruses. J. Virol. *91*, e00503-17. https://doi.org/10.1128/JVI.00503-17.

32. Thamamongood, T., Aebischer, A., Wagner, V., Chang, M.W., Elling, R., Benner, C., García-Sastre, A., Kochs, G., Beer, M., and Schwemmle, M. (2020). A genome-wide CRISPR-cas9 screen reveals the requirement of

host cell sulfation for Schmallenberg virus infection. J. Virol. *94*, e00752-20. https://doi.org/10.1128/JVI.00752-20.

33. Monteiro, J.T., Schon, K., Ebbecke, T., Goethe, R., Ruland, J., Baumgartner, W., Becker, S.C., and Lepenies, B. (2019). The CARD9-associated C-type lectin, mincle, recognizes La Crosse virus (LACV) but plays a limited role in early antiviral responses against LACV. Viruses *11*. https://doi.org/10.3390/v11030303.

34. Plassmeyer, M.L., Soldan, S.S., Stachelek, K.M., Martín-García, J., and González-Scarano, F. (2005). California serogroup Gc (G1) glycoprotein is the principal determinant of pH-dependent cell fusion and entry. Virology *338*, 121–132. https://doi.org/10.1016/j.virol.2005.04.026.

35. Shi, X., Goli, J., Clark, G., Brauburger, K., and Elliott, R.M. (2009). Functional analysis of the Bunyamwera orthobunyavirus Gc glycoprotein. J. Gen. Virol. *90*, 2483–2492. https://doi.org/10.1099/vir.0.013540-0.

36. Bupp, K., Stillmock, K., and González-Scarano, F. (1996). Analysis of the intracellular transport properties of recombinant La Crosse virus glycoproteins. Virology *220*, 485–490. https://doi.org/10.1006/viro.1996.0336.

37. Lappin, D.F., Nakitare, G.W., Palfreyman, J.W., and Elliott, R.M. (1994). Localization of Bunyamwera bunyavirus G1 glycoprotein to the Golgi requires association with G2 but not with NSm. J. Gen. Virol. *75* (*Pt 12*), 3441–3451. https://doi.org/10.1099/0022-1317-75-12-3441.

38. Barbosa, N.S., Mendonça, L.R., Dias, M.V.S., Pontelli, M.C., da Silva, E.Z.M., Criado, M.F., da Silva-Januário, M.E., Schindler, M., Jamur, M.C., Oliver, C., et al. (2018). ESCRT machinery components are required for Orthobunyavirus particle production in Golgi compartments. PLoS Pathog. *14*, e1007047. https://doi.org/10.1371/journal.ppat.1007047.

39. Salanueva, I.J., Novoa, R.R., Cabezas, P., Lopez-Iglesias, C., Carrascosa, J.L., Elliott, R.M., and Risco, C. (2003). Polymorphism and structural maturation of bunyamwera virus in Golgi and post-Golgi compartments. J. Virol. *77*, 1368–1381. https://doi.org/10.1128/jvi.77.2.1368-1381.2003.

40. Shi, X., van Mierlo, J.T., French, A., and Elliott, R.M. (2010). Visualizing the replication cycle of bunyamwera orthobunyavirus expressing fluorescent protein-tagged Gc glycoprotein. J. Virol. *84*, 8460–8469. https://doi.org/10.1128/JVI.00902-10.

41. Bowden, T.A., Bitto, D., McLees, A., Yeromonahos, C., Elliott, R.M., and Huiskonen, J.T. (2013). Orthobunyavirus ultrastructure and the curious tripodal glycoprotein spike. PLoS Pathog. *9*, e1003374. https://doi.org/10.1371/journal.ppat.1003374.

42. Hellert, J., Aebischer, A., Wernike, K., Haouz, A., Brocchi, E., Reiche, S., Guardado-Calvo, P., Beer, M., and Rey, F.A. (2019). Orthobunyavirus spike architecture and recognition by neutralizing antibodies. Nat. Commun. *10*, 879. https://doi.org/10.1038/s41467-019-08832-8.

43. Garry, C.E., and Garry, R.F. (2004). Proteomics computational analyses suggest that the carboxyl terminal glycoproteins of Bunyaviruses are class II viral fusion protein (beta-penetrenes). Theor. Biol. Med. Model. *1*, 10. https://doi.org/10.1186/1742-4682-1-10.

44. Rey, F.A., Heinz, F.X., Mandl, C., Kunz, C., and Harrison, S.C. (1995). The envelope glycoprotein from tick-borne encephalitis virus at 2 A resolution. Nature *375*, 291–298. https://doi.org/10.1038/375291a0.

45. Lescar, J., Roussel, A., Wien, M.W., Navaza, J., Fuller, S.D., Wengler, G., Wengler, G., and Rey, F.A. (2001). The Fusion glycoprotein shell of Semliki Forest virus: an icosahedral assembly primed for fusogenic activation at endosomal pH. Cell *105*, 137–148. https://doi.org/10.1016/s0092-8674(01)00303-8.

46. Dessau, M., and Modis, Y. (2013). Crystal structure of glycoprotein C from Rift Valley fever virus. Proc. Natl. Acad. Sci. USA *110*, 1696–1701. https://doi.org/10.1073/pnas.1217780110.

47. Guardado-Calvo, P., Atkovska, K., Jeffers, S.A., Grau, N., Backovic, M., Pérez-Vargas, J., de Boer, S.M., Tortorici, M.A., Pehau-Arnaudet, G., Lepault, J., et al. (2017). A glycerophospholipid-specific pocket in the RVFV class II fusion protein drives target membrane insertion. Science *358*, 663–667. https://doi.org/10.1126/science.aal2712.

48. Guardado-Calvo, P., Bignon, E.A., Stettner, E., Jeffers, S.A., Pérez-Vargas, J., Pehau-Arnaudet, G., Tortorici, M.A., Jestin, J.L., England, P., Tischler, N.D., and Rey, F.A. (2016). Mechanistic insight into bunyavirus-induced membrane fusion from structure-function analyses of the hantavirus envelope glycoprotein Gc. PLoS Pathog. *12*, e1005813. https://doi.org/10.1371/journal.ppat.1005813.

49. Halldorsson, S., Behrens, A.J., Harlos, K., Huiskonen, J.T., Elliott, R.M., Crispin, M., Brennan, B., and Bowden, T.A. (2016). Structure of a phleboviral envelope glycoprotein reveals a consolidated model of membrane fusion. Proc. Natl. Acad. Sci. USA *113*, 7154–7159. https://doi.org/10.1073/pnas.1603827113.

50. Mishra, A.K., Hellert, J., Freitas, N., Guardado-Calvo, P., Haouz, A., Fels, J.M., Maurer, D.P., Abelson, D.M., Bornholdt, Z.A., Walker, L.M., et al. (2022). Structural basis of synergistic neutralization of Crimean-Congo hemorrhagic fever virus by human antibodies. Science *375*, 104–109. https://doi.org/10.1126/science.abl6502.

51. Willensky, S., Bar-Rogovsky, H., Bignon, E.A., Tischler, N.D., Modis, Y., and Dessau, M. (2016). Crystal structure of glycoprotein C from a hantavirus in the post-fusion conformation. PLoS Pathog. *12*, e1005948. https://doi.org/10.1371/journal.ppat.1005948.

52. Plassmeyer, M.L., Soldan, S.S., Stachelek, K.M., Roth, S.M., Martín-García, J., and González-Scarano, F. (2007). Mutagenesis of the La Crosse Virus glycoprotein supports a role for Gc (1066-1087) as the fusion peptide. Virology *358*, 273–282. https://doi.org/10.1016/j.virol.2006.08.050.

53. Evans, P.R., and Murshudov, G.N. (2013). How good are my data and what is the resolution? Acta Crystallogr. D Biol. Crystallogr. *69*, 1204–1214. https://doi.org/10.1107/S0907444913000061.

54. Adams, P.D., Afonine, P.V., Bunkóczi, G., Chen, V.B., Davis, I.W., Echols, N., Headd, J.J., Hung, L.W., Kapral, G.J., Grosse-Kunstleve, R.W., et al. (2010). PHENIX: a comprehensive Python-based system for macromolecular structure solution. Acta Crystallogr. D Biol. Crystallogr. *66*, 213–221. https://doi.org/10.1107/S0907444909052925.

55. Stubbs, S.H., Cornejo Pontelli, M., Mishra, N., Zhou, C., de Paula Souza, J., Mendes Viana, R.M., Lipkin, W.I., Knipe, D.M., Arruda, E., and Whelan, S.P.J. (2021). Vesicular stomatitis virus chimeras expressing the oropouche virus glycoproteins elicit protective immune responses in mice. mBio *12*, e0046321. https://doi.org/10.1128/mBio.00463-21.

56. Shi, X., Brauburger, K., and Elliott, R.M. (2005). Role of N-linked glycans on bunyamwera virus glycoproteins in intracellular trafficking, protein folding, and virus infectivity. J. Virol. *79*, 13725–13734. https://doi.org/10.1128/JVI.79.21.13725-13734.2005.

57. Pobjecky, N., Smith, J., and Gonzalez-Scarano, F. (1986). Biological studies of the fusion function of California serogroup Bunyaviruses. Microb. Pathog. *1*, 491–501. https://doi.org/10.1016/0882-4010(86)90011-2.

58. Hover, S., Charlton, F.W., Hellert, J., Barr, J.N., Mankouri, J., and Fontana, J. (2022). Organisation of the orthobunyavirus tripodal spike and the structural changes induced by low pH and K+ during entry. Preprint at bioRxiv. https://doi.org/10.1101/2022.08.11.503604.

59. Zhang, Y., and Skolnick, J. (2004). Scoring function for automated assessment of protein structure template quality. Proteins *57*, 702–710. https://doi.org/10.1002/prot.20264.

60. Hastie, K.M., Zandonatti, M.A., Kleinfelter, L.M., Heinrich, M.L., Rowland, M.M., Chandran, K., Branco, L.M., Robinson, J.E., Garry, R.F., and Saphire, E.O. (2017). Structural basis for antibody-mediated neutralization of Lassa virus. Science *356*, 923–928. https://doi.org/10.1126/science.aam7260.

61. Katz, M., Weinstein, J., Eilon-Ashkenazy, M., Gehring, K., Cohen-Dvashi, H., Elad, N., Fleishman, S.J., and Diskin, R. (2022). Structure and receptor recognition by the Lassa virus spike complex. Nature *603*, 174–179. https://doi.org/10.1038/s41586-022-04429-2.

62. Guardado-Calvo, P., and Rey, F.A. (2017). The envelope proteins of the Bunyavirales. Adv. Virus Res. *98*, 83–118. https://doi.org/10.1016/bs.aivir.2017.02.002.

63. Evans, R., O'Neill, M., Pritzel, A., Antropova, N., Senior, A., Green, T., Žídek, A., Bates, R., Blackwell, S., Yim, J., et al. (2022). Protein complex prediction with AlphaFold-Multimer. Preprint at bioRxiv. https://doi.org/10.1101/2021.10.04.463034.

64. Serris, A., Stass, R., Bignon, E.A., Muena, N.A., Manuguerra, J.C., Jangra, R.K., Li, S., Chandran, K., Tischler, N.D., Huiskonen, J.T., et al. (2020). The hantavirus surface glycoprotein lattice and its fusion control mechanism. Cell *183*, 442–456.e16. https://doi.org/10.1016/j.cell.2020.08.023.

65. DuBois, R.M., Vaney, M.C., Tortorici, M.A., Kurdi, R.A., Barba-Spaeth, G., Krey, T., and Rey, F.A. (2013). Functional and evolutionary insight from the crystal structure of rubella virus protein E1. Nature *493*, 552–556. https://doi.org/10.1038/nature11741.

66. Bignon, E.A., Albornoz, A., Guardado-Calvo, P., Rey, F.A., and Tischler, N.D. (2019). Molecular organization and dynamics of the fusion protein Gc at the hantavirus surface. Elife *8*, e46028. https://doi.org/10.7554/eLife.46028.

67. Soldan, S.S., Hollidge, B.S., Wagner, V., Weber, F., and González-Scarano, F. (2010). La Crosse virus (LACV) Gc fusion peptide mutants have impaired growth and fusion phenotypes, but remain neurotoxic. Virology *404*, 139–147. https://doi.org/10.1016/j.virol.2010.04.012.

68. Hollidge, B.S., Salzano, M.V., Ibrahim, J.M., Fraser, J.W., Wagner, V., Leitner, N.E., Weiss, S.R., Weber, F., Gonzalez-Scarano, F., and Soldan, S.S. (2022). Targeted mutations in the fusion peptide region of La Crosse virus attenuate neuroinvasion and confer protection against encephalitis. Viruses *14*. https://doi.org/10.3390/v14071464.

69. Bugnon, P., Breitenmoser, U., Peterhans, E., and Zanoni, R. (2004). Efficacy of oral vaccination in the final stage of fox rabies elimination in Switzerland. J. Vet. Med. Ser. B *51*, 433–437. https://doi.org/10.1111/j.1439-0450.2004.00801.x.

70. Lojkić, I., Šimić, I., Bedeković, T., and Krešić, N. (2021). Current status of rabies and its eradication in eastern and southeastern Europe. Pathogens *10*, 742. https://doi.org/10.3390/pathogens10060742.

71. Yeh, M.T., Bujaki, E., Dolan, P.T., Smith, M., Wahid, R., Konz, J., Weiner, A.J., Bandyopadhyay, A.S., Van Damme, P., De Coster, I., et al. (2020). Engineering the live-attenuated polio vaccine to prevent reversion to virulence. Cell Host Microbe *27*, 736–751.e8. https://doi.org/10.1016/j.chom.2020.04.003.

72. Ariza, A., Tanner, S.J., Walter, C.T., Dent, K.C., Shepherd, D.A., Wu, W., Matthews, S.V., Hiscox, J.A., Green, T.J., Luo, M., et al. (2013). Nucleocapsid protein structures from orthobunyaviruses reveal insight into ribonucleoprotein architecture and RNA polymerization. Nucleic Acids Res. *41*, 5912–5926. https://doi.org/10.1093/nar/gkt268.

73. Figueiredo, L.T.M. (2007). Emergent arboviruses in Brazil. Rev. Soc. Bras. Med. Trop. *40*, 224–229. https://doi.org/10.1590/s0037-86822007000200016.

74. Tilston-Lunel, N.L., Acrani, G.O., Randall, R.E., and Elliott, R.M. (2015). Generation of recombinant oropouche viruses lacking the nonstructural protein NSm or NSs. J. Virol. *90*, 2616–2627. https://doi.org/10.1128/JVI.02849-15.

75. Forshey, B.M., Guevara, C., Laguna-Torres, V.A., Cespedes, M., Vargas, J., Gianella, A., Vallejo, E., Madrid, C., Aguayo, N., Gotuzzo, E., et al. (2010). Arboviral etiologies of acute febrile illnesses in Western South America, 2000-2007. PLoS Neglected Trop. Dis. *4*, e787. https://doi.org/10.1371/journal.pntd.0000787.

76. Manock, S.R., de Bravo, N.B., Smalligan, R.D., Russell, K.L., Espín, J.F., Jacobsen, K.H., Fleming, L.C., Espinoza, W.R., Sanchez, J.L., Kochel, T., et al. (2009). Etiology of acute undifferentiated febrile illness in the Amazon basin of Ecuador. Am. J. Trop. Med. Hyg. *81*, 146–151.

77. Navarro, J.C., Giambalvo, D., Hernandez, R., Auguste, A.J., Tesh, R.B., Weaver, S.C., Montañez, H., Liria, J., Lima, A., Travassos da Rosa, J.F.S., et al. (2016). Isolation of madre de Dios virus (orthobunyavirus; Bunyaviridae), an oropouche virus species reassortant, from a monkey in Venezuela. Am. J. Trop. Med. Hyg. *95*, 328–338. https://doi.org/10.4269/ajtmh.15-0679.

78. Aguilar, P.V., Barrett, A.D., Saeed, M.F., Watts, D.M., Russell, K., Guevara, C., Ampuero, J.S., Suarez, L., Cespedes, M., Montgomery, J.M., et al. (2011). Iquitos virus: a novel reassortant Orthobunyavirus associated with human illness in Peru. PLoS Neglected Trop. Dis. *5*, e1315. https://doi.org/10.1371/journal.pntd.0001315.

79. Baisley, K.J., Watts, D.M., Munstermann, L.E., and Wilson, M.L. (1998). Epidemiology of endemic Oropouche virus transmission in upper Amazonian Peru. Am. J. Trop. Med. Hyg. *59*, 710–716. https://doi.org/10.4269/ajtmh.1998.59.710.

80. Rissanen, I., Stass, R., Krumm, S.A., Seow, J., Hulswit, R.J., Paesen, G.C., Hepojoki, J., Vapalahti, O., Lundkvist, Å., Reynard, O., et al. (2020). Molecular rationale for antibody-mediated targeting of the hantavirus fusion glycoprotein. Elife *9*, e58242. https://doi.org/10.7554/eLife.58242.

81. Jumper, J., Evans, R., Pritzel, A., Green, T., Figurnov, M., Ronneberger, O., Tunyasuvunakool, K., Bates, R., Žídek, A., Potapenko, A., et al. (2021). Highly accurate protein structure prediction with AlphaFold. Nature *596*, 583–589. https://doi.org/10.1038/s41586-021-03819-2.

82. Iwaki, T., Figuera, M., Ploplis, V.A., and Castellino, F.J. (2003). Rapid selection of Drosophila S2 cells with the puromycin resistance gene. Biotechniques *35*, 482–484. https://doi.org/10.2144/03353bm08.

83. Sievers, F., Wilm, A., Dineen, D., Gibson, T.J., Karplus, K., Li, W., Lopez, R., McWilliam, H., Remmert, M., Söding, J., et al. (2011). Fast, scalable generation of high-quality protein multiple sequence alignments using Clustal Omega. Mol. Syst. Biol. *7*, 539. https://doi.org/10.1038/msb.2011.75.

84. Emsley, P., Lohkamp, B., Scott, W.G., and Cowtan, K. (2010). Features and development of Coot. Acta Crystallogr. D Biol. Crystallogr. *66*, 486–501. https://doi.org/10.1107/S0907444910007493.

85. Robert, X., and Gouet, P. (2014). Deciphering key features in protein structures with the new ENDscript server. Nucleic Acids Res. *42*, W320–W324. https://doi.org/10.1093/nar/gku316.

86. Schneider, C.A., Rasband, W.S., and Eliceiri, K.W. (2012). NIH Image to ImageJ: 25 years of image analysis. Nat. Methods *9*, 671–675. https://doi.org/10.1038/nmeth.2089.

87. Sheldrick, G.M. (2010). Experimental phasing with SHELXC/D/E: combining chain tracing with density modification. Acta Crystallogr. D Biol. Crystallogr. *66*, 479–485. https://doi.org/10.1107/S0907444909038360.

88. Crooks, G.E., Hon, G., Chandonia, J.M., and Brenner, S.E. (2004). WebLogo: a sequence logo generator. Genome Res. *14*, 1188–1190. https://doi.org/10.1101/gr.849004.

89. Kabsch, W. (2010). Xds. Acta Crystallogr. D Biol. Crystallogr. *66*, 125–132. https://doi.org/10.1107/S0907444909047337.

90. Weber, P., Pissis, C., Navaza, R., Mechaly, A.E., Saul, F., Alzari, P.M., and Haouz, A. (2019). High-throughput crystallization pipeline at the crystallography core facility of the Institut pasteur. Molecules *24*, 4451. https://doi.org/10.3390/molecules24244451.

91. Schrödinger, L.D.W. (2020). PyMOL [Internet]. http://www.pymol.org/pymol.

92. Fischer, K., Diederich, S., Smith, G., Reiche, S., Pinho Dos Reis, V., Stroh, E., Groschup, M.H., Weingartl, H.M., and Balkema-Buschmann, A. (2018). Indirect ELISA based on Hendra and Nipah virus proteins for the detection of henipavirus specific antibodies in pigs. PLoS One *13*, e0194385. https://doi.org/10.1371/journal.pone.0194385.

STAR★METHODS

KEY RESOURCES TABLE

REAGENT or RESOURCE	SOURCE	IDENTIFIER
Antibodies		
anti-LACV-Gc^{F} mAb 2A3	This study	N/A
anti-mouse Alexa Fluor 488	Invitrogen/Thermo Fisher Scientific	RRID: AB_2534084, Cat# A-11017
anti-mouse Alexa Fluor 594	Invitrogen/Thermo Fisher Scientific	RRID: AB_2534087, Cat# A-11020
Chemicals, peptides, and recombinant proteins		
1:1 v/v mixture of paraffin oil and silicon oil	Hampton Research	Cat# HR3-413
Adjuvant MM	GERBU Biotechnik	Cat# 3001
Effectene transfection reagent	Qiagen	Cat# 301427
Xfect transfection reagent	Takara Bio	Cat# 631318
Insect-XPRESS protein-free medium with L-glutamine	Lonza	Cat# BE12-730Q
penicillin-streptomycin	Gibco	Cat# 15140122
puromycin	Invivogen	Cat# ant-pr-1
polyethylene glycol 1500	Sigma-Aldrich	Cat# P7306
Recombinant protein: LACV Gc^{F} (918–1364) W1066H mutant	This study	RCSB PDB: 7a57
Recombinant protein: LACV Gc^{F} (918–1345)	This study	N/A
Recombinant protein: LACV Gc^{F} (927–1364)	This study	N/A
Recombinant protein: LACV Gc^{S} (477–723)	This study	N/A
Recombinant protein: LACV Gc^{S} (477–911)	Hellert et al.[42]	RCSB PDB: 6h3w
Recombinant protein: SBV Gc^{F} (881–1306)	This study	RCSB PDB: 7a56
Recombinant protein: SBV Gc^{F} (890–1326)	This study	N/A
Critical commercial assays		
Organelle-Lights^{TM} Golgi-GFP BacMam 1.0	Invitrogen/Thermo Fisher Scientific	Cat# O36215
Organelle-Lights^{TM} ER-GFP BacMam 1.0	Invitrogen/Thermo Fisher Scientific	Cat# O36212
Deposited data		
X-ray structure: La Crosse Virus Envelope Glycoprotein Gc W1066H Mutant Fusion Domains in Postfusion Conformation	This study	RCSB PDB: 7a57
X-ray structure: Schmallenberg Virus Envelope Glycoprotein Gc Fusion Domains in Postfusion Conformation	This study	RCSB PDB: 7a56
X-ray structure: Crimean-Congo Hemorrhagic Fever Virus Envelope Glycoprotein Gc W1191H/W1197A/W1199A Mutant in Postfusion Conformation (Monoclinic Crystal Form)	Mishra et al.[50]	RCSB PDB: 7a5a
X-ray structure: Crimean-Congo Hemorrhagic Fever Virus Envelope Glycoprotein Gc W1191H/W1197A/W1199A Mutant in Postfusion Conformation (Orthorhombic Crystal Form)	Mishra et al.[50]	RCSB PDB: 7a59
X-ray structure: CCHFV Gc prefusion monomer bound to ADI-36121 and ADI-37801 Fabs	Mishra et al.[50]	RCSB PDB: 7l7r
X-ray structure: Structure of hantavirus envelope glycoprotein Gc in postfusion conformation	Guardado-Calvo et al.[48]	RCSB PDB: 5ljz
X-ray structure: Structure of RVFV envelope protein Gc in postfusion conformation in complex with 1,2-dipropionyl-sn-glycero-3-phosphocholine	Guardado-Calvo et al.[47]	RCSB PDB: 6egu

(*Continued on next page*)

Continued

REAGENT or RESOURCE	SOURCE	IDENTIFIER
Cryo-ET structure: Model of the Rift Valley fever virus glycoprotein hexamer type 1	Halldorsson et al.[49]	RCSB PDB: 6f9c
Previously available amino acid sequences	GenBank	see method details: Position-specific sequence similarity plots
Experimental models: Cell lines		
Drosophila S2	Gibco/Thermo Fisher Scientific	Cat# R690-07
BHK-21/BSR-T7/5	Collection of Cell Lines in Veterinary Medicine, FLI, Germany	Cat# CCLV-RIE 0583
RK-13	Collection of Cell Lines in Veterinary Medicine, FLI, Germany	Cat# CCLV-RIE 0109
SP2/0	Collection of Cell Lines in Veterinary Medicine, FLI, Germany	Cat# CCLV-RIE 0223
Experimental models: Organisms/strains		
female BALB/c mice	Specific pathogen-free breeding unit of the Friedrich-Loeffler-Institut, Germany	N/A
Recombinant DNA		
pCMV BAD C-HA vector	Invitrogen/Thermo Fisher Scientific	Cat# 82028
pCoPURO plasmid	Iwaki et al., 2003[82]	Addgene #17533
pEXPR-IBA103 vector	iba Life Science	Cat# 2-3503-000
pMT vector	Invitrogen/Thermo Fisher Scientific	Cat# V412020
Software and algorithms		
Aimless	Evans and Murshudov[53]	https://www.ccp4.ac.uk/html/aimless.html
AlphaFold-Multimer	Evans et al.[63]	https://www.deepmind.com
ASTRA	Wyatt Technology	https://www.wyatt.com/products/software/astra.html
Clustal Omega web server	Sievers et al.[83]	https://www.ebi.ac.uk/Tools/msa/clustalo/
Coot	Emsley et al.[84]	https://www2.mrc-lmb.cam.ac.uk/personal/pemsley/coot/
ESPript 3.0 web server	Robert and Gouet[85]	https://espript.ibcp.fr/
ImageJ version 1.48	Schneider et al.[86]	https://imagej.nih.gov/ij/
Phenix	Adams et al.[54]	https://phenix-online.org/
Prism version 6	GraphPad	https://www.graphpad.com/
PyMOL version 2.4	Schrodinger, LLC	https://pymol.org/2/
SHELXE	Sheldrick[87]	http://www.csb.yale.edu/userguides/datamanip/shelx/shelx.htm
STARANISO web server	Global Phasing Ltd.	https://staraniso.globalphasing.org/
WebLogo web server	Crooks et al.[88]	https://weblogo.berkeley.edu/logo.cgi
XDS	Kabsch[89]	https://xds.mr.mpg.de/
Other		
8-well Lab-Tek chamber-slides	Thermo Fisher Scientific	Cat# 177402
10 kDa MWCO PES membrane	Sartorius	Cat# VF20P0
10 kDa MWCO PES Vivaspin centrifugal concentrator	Sartorius	Cat# VS2001
siliconized glass slides	Hampton Research	Cat# HR3-231
Strep-Tactin Superflow hc column	iba Life Science	Cat# 2-1238-001
Superdex 200 10/300 column	GE Healthcare	Cat# 17-5175-01
HiLoad Superdex 200 pg column	GE Healthcare	Cat# 28-9893-35

RESOURCE AVAILABILITY

Lead contact

Further information and requests for resources and reagents may be directed to and will be fulfilled by the lead contact Félix A. Rey (felix.rey@pasteur.fr).

Materials availability

The monoclonal anti-LACV-Gc^F antibody 2A3 can be obtained through a material transfer agreement (MTA) from the Friedrich-Loeffler-Institut.

Data and code availability

- Atomic coordinates, structure factor amplitudes, and the respective protein sequences have been deposited to the Protein DataBank (PDB). Accession numbers are PDB: 7a56 for the atomic model of SBV Gc(881–1306) and PDB: 7a57 for LACV Gc(918–1364). This paper also analyzes existing, publicly available structural data, the accession numbers for which are listed in the key resources table.
- This study did not require developping any novel code.
- Any additional information required to reanalyze the data reported in this paper is available from the lead contact upon request.

EXPERIMENTAL MODEL AND SUBJECT DETAILS

Animals

The monoclonal anti-LACV-Gc^F antibody 2A3 was produced using two female BALB/c mice (Specific pathogen-free breeding unit of the Friedrich-Loeffler-Institut, Germany) at an age of nine weeks at the onset of the experiment. The experiment was carried out in line with the national and European legislation, with approval by the competent authority of the Federal State of Mecklenburg-Western Pomerania, Germany (reference number: 7221.3-2-042/17).

Cell lines

Drosophila S2 cells (Gibco/Thermo Fisher Scientific; Cat# R690-07) for recombinant protein production were grown in Insect-XPRESS protein-free medium with L-glutamine (Lonza; Cat# BE12-730Q) supplemented with 25 U/mL penicillin-streptomycin (Gibco/Thermo Fisher Scientific; Cat# 15140122) at 28°C. SP2/0 - Ag12 myeloma cells (Collection of Cell Lines in Veterinary Medicine, FLI, Germany; Cat# 0223) for hybridoma generation were grown in RPMI-1640 medium with 10% fetal calf serum, 1× MEM non-essential amino acids, 2 mM L-glutamine, and 1 mM sodium pyruvate. RK-13 cells (Collection of Cell Lines in Veterinary Medicine, FLI, Germany; Cat# 0109) for the cell-cell-fusion assay were grown in MEM with 10% fetal calf serum. BHK-21/BSR-T7/5 cells (Collection of Cell Lines in Veterinary Medicine, FLI, Germany; Cat# 0583) for relative quantification of Gc expression on the cell surface were grown in Glasgow's MEM supplemented with tryptose phosphate and 10% fetal calf serum. All mammalian cell lines were grown at 37°C and 5% CO_2. All mammalian cells were authenticated by species-specific PCR and by genotyping using short tandem repeat (STR) analysis.

METHOD DETAILS

Recombinant protein production

Recombinant Gc fragments with an N-terminal Strep tag (sequence: EWSHPQFEKGG) were produced in *Drosophila* S2 cells (Gibco/Thermo Fisher Scientific; Cat# R690-07) expressing codon-optimized synthetic genes (Invitrogen/Thermo Fisher Scientific) downstream of a BiP secretion signal from the pMT vector (Invitrogen/Thermo Fisher Scientific; Cat# V412020). Cells were grown in Insect-XPRESS protein-free medium with L-glutamine (Lonza; Cat# BE12-730Q) supplemented with 25 U/mL penicillin-streptomycin (Gibco; Cat# 15140122) at 28°C. Expression plasmids were co-transfected with the selection plasmid pCoPURO[82] at a mass ratio of 20:1 using the Effectene transfection reagent (Qiagen; Cat# 301427) according to the manufacturer's instructions. Polyclonal stable S2 cell lines were established by selection with 7.5 μg/mL puromycin (Invivogen; Cat# ant-pr-1), which was added to the medium 40 h after transfection. Cultures were expanded to 1 L of 10^7 cells/mL in Erlenmeyer flasks shaking at 100 rpm at 28°C. Recombinant protein expression was then induced with 5 μM $CdCl_2$. Cell supernatants were harvested one week after induction, concentrated to 50 mL on a 10 kDa MWCO PES membrane (Sartorius; Cat# VF20P0), pH-adjusted with 0.1 M Tris-Cl pH 8.0, cleared from biotin with 15 μg/mL avidin, cleared from precipitate by centrifugation at 4000 × g for 15 min at 8°C, and applied to affinity purification on a 5 mL Strep-Tactin Superflow hc column (iba Life Science; Cat# 2-1238-001). Trimeric protein was separated from monomeric protein by gel permeation chromatography on a HiLoad Superdex 200 pg column (GE Healthcare; Cat# 28-9893-35) in 20 mM Tris-Cl pH 8.0, 150 mM NaCl. Protein concentrations were adjusted in 10 kDa MWCO PES Vivaspin centrifugal concentrators (Sartorius; Cat# VS2001).

Crystallization

The SBV Gc fragment comprised residues 881–1306 of the polyprotein precursor (isolate BH80, GenBank: CCF55030). Initial crystal screening was performed at the macromolecular crystallization platform of the Institut Pasteur.[90] Optimal crystals were obtained by the hanging-drop vapor diffusion method: 0.5 μL of 4.5 mg/mL trimeric SBV Gc fragment in 20 mM Tris-Cl pH 8.0, 150 mM NaCl were added to 0.5 μL of reservoir solution containing 20% w/v PEG 1K, 0.1 M Na/K phosphate pH 6.2 and 0.2 M NaCl. The drops were equilibrated against reservoir solution on siliconized glass slides (Hampton Research; Cat# HR3-231) for two weeks at 18°C. Crystals were cryo-protected in 20% v/v PEG 400, 16% w/v PEG 1K, 80 mM Na/K phosphate pH 6.2, 160 mM NaCl prior to conservation in liquid nitrogen. Iodide derivate samples for SAD phasing were prepared by incubating native crystals in a drop containing 0.6 M NaI, 27% v/v PEG 400, 57 mM sodium acetate and 57 mM MES pH 6.5 over night before cryo-cooling without back-soaking.

The LACV Gc fragment comprised residues 918–1364 of the polyprotein precursor (isolate L78, GenBank: ABQ12634), and the W1066H mutation was introduced into the *cd* loop in order to obtain soluble trimers suitable for crystallization. After initial crystal screening, the optimal crystals were obtained by the sitting-drop vapor diffusion method: 0.2 μL of 8.5 mg/mL trimeric LACV Gc(918–1364) W1066H in 20 mM Tris-Cl pH 8.0, 150 mM NaCl were added to 0.2 μL of reservoir solution containing 0.1 M Bis-Tris propane pH 7 and 1.2 M K/Na tartrate (final pH: 8.0). The drops were equilibrated against reservoir solution two weeks at 18°C. Crystals were cryo-protected in a 1:1 v/v mixture of paraffin oil and silicon oil (Hampton Research; Cat# HR3-413) prior to flash freezing in liquid nitrogen.

X-Ray data collection and structure determination

Native high-resolution X-ray diffraction data were recorded at synchrotron beamline ID23-2 at the ESRF with a PILATUS3 X 2M detector for SBV Gc(881–1306) and at beamline PX1 at SOLEIL with a PILATUS 6M detector for LACV Gc(918–1364) W1066H. Both datasets were processed with XDS[89] and Aimless.[53] The LACV dataset was truncated anisotropically using the STARANISO web server (Global Phasing Ltd.) (Table 1). An ellipsoid was fitted to the anisotropic cut-off surface to provide approximate resolution limits along three directions in reciprocal space, although the real cut-off surface is only approximately ellipsoidal, and the directions of the worst and best resolution limits may not correspond with the reciprocal axes.

The structure of SBV Gc(881–1306) was determined by SAD phasing. An iodide derivate dataset of 294° (oscillation angle: 1°) was collected from a single crystal on our in-house Rigaku MicroMax 007 X-ray generator with a standard rotating anode (wavelength 1.54 Å) in combination with a Marresearch Mar345dtb image plate detector. The derivative dataset was processed with XDS[89] and Aimless.[53] Significant anomalous signal reached to a resolution of 3.3 Å, and SAD phasing was carried out with SHELXE.[87] The initial density map was readily interpretable through iterative manual model building in Coot[84] and automatic refinement in Phenix.Refine.[54] Phases were extended to the high-resolution native dataset in Phenix.MR.[54] The structure of LACV Gc(918–1364) W1066H was subsequently determined by molecular replacement with the SBV structure using Phenix.MR followed by iterative manual and automated modeling in Coot and Phenix.Refine. The final crystallographic statistics and the PDB deposition codes of the atomic coordinates and structure factors are shown in Table 1. All structure representations were composed in PyMOL[91] version 2.4.

Structural comparisons

The structural comparisons presented in Figure 4 were done using the atomic models for LACV Gc^F (PDB: 7a57, this work) representing the *Orthobunyavirus* genus; CCHFV Gc (PDB: 7a59), representative of the Orthonairovirus genus; RVFV Gc (PDB: 6egu), representative of the *Phlebovirus* genus; and HTNV Gc (PDB: 5ljz), representative of the *Orthohantavirus* genus. In the analysis of the rmsd and TM-score upon structural alignment of the individual domains, we used SBV Gc (PDB: 7a56, this work) instead of LACV Gc as representative of the *Orthobunyavirus* genus, because of the higher resolution of this structure (see Table 1)

Multi-angle static light scattering

Purified recombinant proteins at concentrations of 1 mg/mL were subjected to size exclusion chromatography on a Superdex 200 10/300 column (GE Healthcare; Cat# 17-5175-01) equilibrated in 20 mM Tris-Cl, 150 mM NaCl, pH 8.0. Separations were performed at 20°C with a flow rate of 0.5 mL/min. Online multi-angle static light scattering analysis was performed with a Wyatt DAWN-HELEOS II detector. Online differential refractive index measurements were performed with a Wyatt Optilab T-rEX detector. Data were analyzed using the ASTRA software (Wyatt Technology).

Generation of monoclonal antibody 2A3

Monomeric LACV Gc(477–1364) was purified from recombinant *Drosophila* S2 cell supernatants as described above. The protein was used to immunize two six-weeks-old female BALB/c mice intraperitoneally using four doses of 50 μg each mixed with an equal amount of GERBU Adjuvant MM (GERBU Biotechnik; Cat# 3001) in 4-week intervals. Four days after the final boost, the immunized mice were euthanized and the splenocytes were fused with SP2/0 - Ag12 myeloma cells (Cell Culture Collection of the Friedrich-Loeffler-Institut, Germany; Cat# 0223) at a ratio of 1:4 in the presence of polyethylene glycol 1500 (Sigma-Aldrich; Cat# P7306). Hybridoma cells were selected and cloned following a standard protocol.[92] The experiment was carried out in line with the national and European legislation, with approval by the competent authority of the Federal State of Mecklenburg-Western Pomerania, Germany (reference number: 7221.3-2-042/17).

Hybridoma supernatants were screened for reactivity with the immunization antigen in indirect ELISA. Hybridomas producing antigen-specific antibodies were sub-cloned twice by limited dilution and their specificity was further narrowed down using a panel of recombinant Gc fragments in indirect ELISA. One of the resulting monoclonal antibodies, 2A3, which was used for immunofluorescent staining in this work, reacted with monomeric wild-type Gc^F (Gc aa 927–1364), trimeric wild-type Gc^F (aa 918–1345) and trimeric W1066H mutant Gc^F (aa 918–1364), but not with the Gc^S fragments aa 477–723 and 477–911.

Cell-cell fusion assay

The complete LACV polyprotein precursor of the viral M segment or its mutants Δ(F478-E927), Δ(F478-Y949), L944D, T1042A, T1042D, W1066A, F1071A, L1074A, L1194A and L1194D were expressed from a codon-optimized synthetic gene (Invitrogen/Thermo Fisher Scientific) in the mammalian expression vector pEXPR-IBA103 (iba Life Science; Cat# 2-3503-000). EGFP was expressed from pCMV-eGFP, which is based on the mammalian expression vector pCMV BAD C-HA (Thermo Fisher Scientific; Cat# 82028).

RK-13 cells (Collection of Cell Lines in Veterinary Medicine, FLI, Germany; Cat# 0109) were seeded into 24-well plates in MEM with 10% FCS one day prior to transfection. 70–80% confluent cells were transfected with 3.0 μg of pEXPR-IBA103 expressing wild-type or mutant LACV polyprotein precursor together with 0.5 μg of pCMV-eGFP using Xfect transfection reagent (Takara Bio; Cat# 631318) following the manufacturer's recommendations at a ratio of 1.0 μL Xfect/3.5 μL DNA. Cell-cell fusion was induced 24 h post-transfection by incubation with pH-adjusted fusion medium (MEM +10% FCS, 10 mM HEPES, 10 mM MOPS) for 10 min at room temperature. The fusion medium was subsequently replaced with fresh medium (neutral pH with 10% FCS). After incubation for 5 h at 37°C and 5% CO_2, the cells were fixed with 4% PFA for 20 min at room temperature and were subsequently permeabilized with 0.5% Triton X-100 for 5 min. Immunofluorescence staining was performed using monoclonal antibody 2A3 diluted 1:2 in PBS, 0.05% Tween, pH 7.4 in combination with an anti-mouse Alexa Fluor 594 secondary antibody (Invitrogen/Thermo Fisher Scientific; Cat# A-11020) for detection. Nuclei were stained with DAPI.

Immunofluorescence images were taken on a Nikon Eclipse Ti-U inverted microscope. For each construct and each pH condition, 1,000 nuclei in Gc- and GPF-positive cells were counted per well in biological triplicates. Counts of cells and nuclei were recorded using the NIS-Elements Imaging Basic Research software (Nikon). Fusion indices were calculated using the formula: 1 – [number of cells/number of nuclei].[48]

Gc surface expression

Gc surface expression was quantified on BHK-21/BSR-T7/5 cells (Collection of Cell Lines in Veterinary Medicine, FLI, Germany; Cat# 0583), which form confluent layers of evenly distributed cells that are ideal for immunofluorescence analysis. Cells were seeded into 8-well Lab-Tek chamber-slides (Thermo Fisher Scientific; Cat# 177402). 24 h after seeding, they were transfected with 1 μg of pEXPR-IBA103 expressing wild-type or mutant LACV polyprotein precursor using Xfect transfection reagent (Takara Bio; Cat# 631318) following the manufacturer's recommendations. 4–5 h after transfection, the medium was replaced with fresh medium supplemented with 5% FCS, and the cells were incubated for 24 h at 37°C and 5% CO_2. Monoclonal antibody 2A3, diluted 1:2 in MEM without FCS, was incubated with unfixed cells for 1 h at room temperature. The cells were subsequently fixed with 4% PFA for 20 min at room temperature, washed with PBS +0.05% Tween and then incubated with an anti-mouse Alexa Fluor 488 secondary antibody (Invitrogen/Thermo Fisher Scientific; Cat# A-11017). Finally, the cells were permeabilized with 0.5% Triton X-100 and the nuclei were stained with DAPI.

Immunofluorescence imaging was performed using the NIS-Elements Imaging Basic Research software (Nikon) on a Nikon Eclipse Ti-U inverted microscope. For each well, three images were recorded with identical exposure parameters and background corrections. The RGB FITC values of each image were determined using ImageJ version 1.48(ref. 86). Mean values of three images per construct were considered as one replicate value. The experiment was performed in biological triplicates.

Co-localization of Gc with cellular compartments

RK-13 cells (Collection of Cell Lines in Veterinary Medicine, FLI, Germany; Cat# 0109) were seeded onto 20 mm coverslips and were incubated overnight. 80–90% confluent cells were transfected with 4.5 μg of pEXPR-IBA103 expressing wild-type or mutant LACV polyprotein precursor and subsequently incubated for 4 h at 37°C. After washing with MEM without FCS, the cells were transduced with the GFP-expressing baculoviruses Organelle-Lights Golgi-GFP BacMam 1.0 (Invitrogen/Thermo Fisher Scientific; Cat# O36215) or Organelle-Lights ER-GFP BacMam 1.0 (Invitrogen/Thermo Fisher Scientific; Cat# O36212) targeting the Golgi compartment or the ER respectively, following the manufacturer's instructions. The cells were incubated with baculovirus preparations diluted in MEM +10% FCS for 3 h at 37°C and were subsequently washed and supplemented with fresh medium (5% FCS). After incubation for 24 h at 37°C, the cells were fixed with 4% PFA and permeabilized with 0.5% Triton X-100. Immunofluorescence staining was performed using monoclonal antibody 2A3 diluted 1:2 in PBS +0.05% Tween in combination with an anti-mouse Alexa Fluor 594 secondary antibody (Invitrogen/Thermo Fisher Scientific; Cat# A-11020). Nuclei were stained with DAPI. Immunofluorescence images were recorded using a 100× oil immersion objective lens on a Nikon Eclipse Ti-U inverted microscope.

AlphaFold prediction

Prediction of the trimeric LACV Gc^F structure was carried out using a local installation of AlphaFold-Multimer[63] using the protein databank released August 1st 2021, which did not yet include our experimental structures. The best prediction obtained is the one displayed in Figure S5, providing the program the aa sequence spanning residues 927–1364 (displayed in Figure 2D), corresponding to the atomic model of out experimental X-ray structure.

Position-specific sequence similarity plots

The sequence similarity data plotted in Figure 4B were calculated using the ESPript 3.0 web server.[85] The data were averaged over a window of 15 residues to smoothen the plot. Sequence logos were calculated using the WebLogo web server.[88] The underlying multiple sequence alignments were prepared with Clustal Omega[83] using the following GenBank entries.

Orthobunyavirus. La Crosse virus (GenBank: AAM94388), Bwamba virus (GenBank: AIN37029), Gamboa virus (GenBank: AIS74641), Alajuela virus (GenBank: AIS74643), Umbre virus (GenBank: KP792686), Guaroa virus (GenBank: AAR28442), Wyeomyia virus (GenBank: AGA54137), Bunyamwera virus (GenBank: AAA42777), Kairi virus (GenBank: A0A161CGA5), Main Drain virus (GenBank: ABV68910), Nyando virus (GenBank: AIN37030), Wolkberg virus (GenBank: YP_009362985), Kaeng Khoi virus (GenBank: AIN37035), Zegla virus (GenBank: AXP33568), Patois virus (GenBank: AXP33566), Mirim virus (GenBank: APM83099), Guajara virus (GenBank: KP792662), Capim virus (GenBank: KT160027), Guama virus (GenBank: KP792665), Catu virus (GenBank: KP792659), Bimiti virus (GenBank: KP792656), Madrid virus (GenBank: AGW82139), Caraparu virus (GenBank: AGW82158), Marituba virus (GenBank: AGW82142), Oriboca virus (GenBank: AGW82131), Tete virus (GenBank: KP792680), Thimiri virus (GenBank: AXP32071), Manzanilla virus (GenBank: AHY22343), Oropouche virus (GenBank: A0A0D4BSW3), Shuni virus (GenBank: ALK26467), Schmallenberg virus (GenBank: CCF55030), Simbu virus (GenBank: YP_006590085), Shamonda virus (GenBank: AB698475), Akabane virus (GenBank: AB568603), Tacaiuma virus (GenBank: ASY08210), Anopheles A virus (GenBank: ATJ04175).

Orthonairovirus. Crimean-Congo hemorrhagic fever virus (GenBank: AAM48106), Hazara virus (GenBank: ABH07417), Dugbe virus (GenBank: AMT75393), Nairobi sheep disease virus (GenBank: AIZ00431), Thiafora virus (GenBank: ALD84356), Artashat virus (GenBank: AKC89353), Sakhalin virus (GenBank: AMT75420), Keterrah virus (GenBank: ALD84353), Kasokero virus (GenBank: ALD84350), Chim virus (GenBank: AKC89344), Qalyub virus (GenBank: KU343161), Tamdy virus (GenBank: AKC89326), Hughes virus (GenBank: AMT75408), Dera Ghazi Khan virus (GenBank: AMT75390).

Orthohantavirus. Hantaan virus (GenBank: AAA43836), Dabieshan virus (GenBank: AFG26308), Sangassou virus (GenBank: AEZ02947), Dobrava-Belgrade virus (GenBank: CAC85164), Thailand virus (GenBank: AAA16239), Seoul virus (GenBank: AAA47825), Bruges virus (GenBank: AOC84247), Bowe virus (GenBank: AGW23848), Jeju virus (GenBank: YP_009361850), Oxbow virus (GenBank: ACT68338), Cao Bang virus (GenBank: ABR29829), Asama virus (GenBank: ACI28508), Kenkeme virus (GenBank: AIL25322), Amga virus (GenBank: AID54673), Yakeshi virus (GenBank: YP_009507845), Asikkala virus (GenBank: AGK36761), Rockport virus (GenBank: AEA11485), Fugong virus (GenBank: YP_009362033), Luxi virus (GenBank: ADV33303), Prospect Hill virus (GenBank: CAA38922), Tula virus (GenBank: NP_942586), Puumala virus (GenBank: AAC37848), Fusong-Mf-682 virus (GenBank: ABV80308), Khabarovsk virus (GenBank: CAB42088), El Moro Canyon virus (GenBank: AAA87198), Montano virus (GenBank: BAK08520), Sin Nombre virus (GenBank: AIA08876), Bayou virus (GenBank: AAA61690), Cano Delgadito virus (GenBank: ABB88646), Choclo virus (GenBank: ABB90558), Maporal virus (GenBank: AAR14889), Necocli virus (GenBank: AHJ38538), Andes virus (GenBank: AAO86638), Laguna Negra virus (GenBank: AAB87603).

Phlebovirus. Rift Valley Fever virus (GenBank: AAA47450), Joa virus (GenBank: API68885), Punta Toro virus (GenBank: AAA47110), Chandiru virus (GenBank: AEA30045), Bujaru virus (GenBank: API68881), Salehabad virus (GenBank: AGA82742), Sandfly fever Naples virus (GenBank: AEL29667).

QUANTIFICATION AND STATISTICAL ANALYSIS

All data are represented as means ± SD. Statistical analysis of LACV Gc surface expression compared to non-transfected cells was performed in GraphPad Prism 6 using one-way ANOVA followed by Dunnett's multiple comparisons test with $\alpha = 0.05$.